FINAL REPORT

Advanced Space-Based InSAR Risk Analysis of Planned and Existing Transportation Infrastructure

Award # OASRTRS-14-H-SUI

21-MAR-17

Submitted by:

Stanford University and MDA Geospatial Services

PIs: Stanford University: Howard Zebker, zebker@stanford.edu, MDA: Mary Anne McParland

Documents also prepared by:

Mike Kubanski, Fernando Greene, Jayson Eppler, MDA

Final report prepared by Stanford University

Executive Summary and Objectives of Work

Summary:

This report documents the work completed under the above agreement. We first summarize the project objectives, activities, and deliverables and show that all items have been addressed, although we were not able to successfully meet with all our desired state DOTs due to lack of schedule availability at the agencies. We were able to complete all technical work as proposed. Technical details from Stanford, MDA, and our soil engineer follow after the programmatic review.

Project Objectives:

- To assemble an operational prototype of a powerful space-borne Synthetic Aperture Radar Interferometry (InSAR) displacement monitoring system
- Work, with participating state DOTs, towards integrating this system with current risk assessment practices of existing and planned road and bridge infrastructure.

TABLE OF CONTENTS

LIST OF TABLES

ACRONYMS AND ABBREVIATIONS

2D	Two-Dimensional
Asc	Ascending
CalTrans	California Department of Transportation
DEM	Digital Elevation Model
Des	Descending
DOT	Department of Transportation
GIS	Geographic Information System
GUI	Graphical User Interface
HDS-InSAR	Homogeneous Distributed Scatterer-InSAR
InSAR	Interferometric Synthetic Aperture Radar
KML	Keyhole Markup Language
LiDAR	Light Detection and Ranging
LOS	Line-of-Sight
MDA	MDA Geospatial Services Inc.
MSE	Mechanically Stabilized Earth
NED	National Elevation Dataset
NOAA	National Oceanic and Atmospheric Administration
PennDOT	Pennsylvania Department of Transportation
SAR	Synthetic Aperture Radar
SHP	Shapefile
SLA	Spotlight (RADARSAT-2 mode)
SRTM	Shuttle Radar Topography Mission
UI	User Interface
USDOT	US Department of Transportation
USGS	United States Geological Survey
WSDOT	Washington State Department of Transportation

1 INTRODUCTION

1.1 Purpose

The purpose of this document is to summarize activities by Stanford University and MDA Geospatial Services Inc. (MDA) to estimate surface deformation and associated risk to transportation infrastructure using SAR Interferometric methods for the Advanced Space-Based Interferometric Synthetic Aperture Radar (InSAR) Risk Analysis of Planned and Existing Transportation Infrastructure project.

1.2 Scope of the Document

This report includes a description of InSAR analysis performed for all four project study sites and summarizes the final results obtained. This report also summarizes InSAR method improvements implemented during the project, plus the development of an enhanced Google Earth InSAR visualization plug-in. Stakeholder InSAR workshops were conducted with both the Washington State Department of Transportation (WSDOT) and Pennsylvania Department of Transportation (PennDOT). Summaries of those workshops are detailed in a separate report.

1.3 Target Audience

This document is intended for the project teams at Stanford University and MDA and for the USDOT and for the project end users who include WSDOT, PennDOT and the California Department of Transportation (CalTrans).

THIS PAGE INTENTIONALLY LEFT BLANK

2 ACTIVITY AND DELIVERABLES SUMMARY

2.1 Activities

We list each activity with its final status. Details appear in the technical sections follow below. The activities proposed were:

1. Kick-off meeting with the project team to review the project objectives and activities and modify as necessary. (Completed)
2. At the start of project, seek input from State DOTs on the project activities, specifically to determine experiment sites and required analyses. (Completed with the states of Pennsylvania and Washington, California was too busy to provide input)
3. Setup and maintain a project website (Completed)
4. Plan and order archived and new RADARSAT-2 data sets required by the project (Completed)
5. Conduct dual scale point scatterer analysis over selected test sites (Completed)
6. Develop Radarsat interface software for Stanford InSAR processor (Completed)
7. Study deformation of ground surface over selected test sites. (Completed)
8. Develop tools that visualize InSAR analysis results in a manner that can be interpreted and exploited by State DOTs. (Completed)

9. Organize Workshops at which project final results will be presented to State DOTs and their feedback obtained. (Completed with Pennsylvania, informally with Washington, California cancelled the workshop just before its scheduled date)
10. Prepare a final report documenting the methodology, the results, feedback from the State DOTs, project conclusions and recommendations for follow on activities. (This report)
11. Attend project review meetings with US DOT (Completed by telephone and quarterlky documentation)
12. Publish papers on the results of the project in the open literature. (Papers in process and will appear according to publication schedules)

2.2 Deliverables summary

The following deliverables were all met with several satisfied by this report.

1. Minutes from the Kick-off meeting including action items and a description of any modifications to the project plan. Minutes due to DOT within three (3) months of the effective date of the Agreement (Del – 1A).

2. Technical report summarizing requirements and needs specific to State DOT partners, including experiment sites, measurements, and analyses. Report due to DOT within three (3) months of the effective date of the Agreement (Del – 2A).

3. Conduct dual scale point scatterer analysis over selected test sites. Report on results due to DOT within twelve (12) months of the effective date of the Agreement (Del – 3A).

4. Study deformation of ground surface over selected test sites. Report on results due to DOT within twenty-one (21) months of the effective date of the Agreement (Del – 4A).

5. Report describing tools that visualize InSAR analysis results in a manner that can be interpreted and exploited by State DOTs. Report on results due to DOT within twenty-one (21) months of the effective date of the Agreement (Del – 5A).

6. Report summarizing feedback from the State DOTs on the project technical results presented to them at Workshops. Report on results due to DOT within twenty-four (24) months of the effective date of the Agreement (Del – 6A).

7. Quarterly Progress Reports briefly describing progress over the last quarter, activities planned for the next quarter, budget and schedule status and any problems arising along with resolution plan (QPR 1-8).

8. Project website for public dissemination of project results

9. Final Report summarizing the project methodology and results, project conclusions and recommendations for follow on activities (FR-1). Includes papers submitted to conference presentations and publication in peer review journals.

10. Financial reports as required by US DOT.

2.3 Budget and cost match

The cost match for this project consisted of high-value SAR data sets offered to DOT at a small fraction of list cost. As data are delivered and inspected at Stanford, we credit the cost match in a specific account managed by Stanford's financial group. Delivery of data sets is now complete. Some data were delivered rather late in the process so we have not had a chance to analyze everything, however the technical section below summarizes the results from the data received. The cost match objective has been met.

THIS PAGE INTENTIONALLY LEFT BLANK

3 APPROACH AND METHODOLOGY

3.1 Background

1. The flexibility and robustness of the advanced InSAR methods contained in this system make it adaptable to specific infrastructure problems and particular environments throughout the United States. The system is thus expected to allow partnering State DOTs to greatly reduce their costs and improve the timeliness for monitoring new and existing transportation infrastructure. Cost benefits above the status-quo of road infrastructure monitoring are achieved through the system's superior spatial coverage allowing timely reconnaissance monitoring and identification of problem hotspots to efficiently direct on-the-ground monitoring to where it is warranted.
2. Over the last few years Stanford University and MDA, have developed independently a suite of cutting edge algorithms to derive mm-level surface displacement from spaceborne InSAR imagery. We propose to combine our expertise synergistically in a "best of" and complementary way towards prototyping a comprehensive InSAR displacement monitoring system. The proposed research is conducted in close collaboration with State DOTs to guide the evolving prototype to providing efficient and robust unstable ground risk analysis in the planning phase of new transportation infrastructure as well as monitoring the stability and integrity of existing infrastructure.

3.2 Main Technical Accomplishments

Each item below addresses a specific project task as listed in the proposal Attachment 1 (tasks) and a specific deliverable as listed in proposal Attachment 2 (deliverables) of the cooperative agreement. The particular task and deliverable addressed are noted as Task N and Deliverable M corresponding to the numbered items in the proposal attachments.

- We engaged two graduate students, Ann Chen and Karissa Cristiano, to move forward on this work. Karissa initially supported the project before her graduation from our MS program. Ann is an expert in InSAR processing and has identified several areas in the Pennsylvania images where there is possible subsidence. She is implementing

some detailed deformation analysis and deriving time series of the surface displacements for these regions. In this past period she has been reducing the data from the two Pennsylvania sites. (tasks 6 and 7, deliverable 4)

• We also engaged a civil engineer, Prof. Venkat Lakshmi of the University of South Carolina, to help analyze soil conditions as suggested by the InSAR time series. His expertise is in water systems and hydrology and is studying the data for road degradation, present and expected. His report is attached below. (task 7, deliverable 4)

• Graduate student Chen along with Lakshmi facilitated the interpretation of the Seattle and Pennsylvania scenes. Chen produced time series and the two have been examining the data to to understand the causes of observed subsidence in the two areas. (task 7, deliverable 4)

• We completed the Stanford work in the graduate student training and analysis of the Seattle and Los Angeles sites using existing data sets. Chen has reprocessed and extended all of the time series generated in previous periods. (tasks 4, 6, 7, deliverables 4, 9)

• MDA has continued development of visualization tools and explored their use with state DOT representatives, will schedule workshops to encourage technology transfer. (tasks 3, 5, deliverable 9)

• Other details of MDA progress listed after this introductory section of report (see below)

3.3 Other Objectives: Interface with State DOTs

Another major item on the agenda was to hold the technology transfer meetings with the state DOTs in Washington and Pennsylvania. California declined to participate, in fact cancelling our scheduled workshop just before it was to begin due to internal prioritization. MDA did schedule the WA and PA symposia, and took the lead in organizing these meetings and handing the direct technology transfer.

3.4 Technical summary: general methodological improvements

Detecting localized road damage due to sinkholes induced by engineering projects using high resolution RADARSAT-2 data

Jingyi Chen, Howard Zebker, Venkat Lakshmi and Karissa Cristiano

3.4.1. Research Motivation

Karst topography can be found in all 50 states in the US. The dissolution of carbonates rocks such as limestone and dolomite lead to voids in the bedrock. As soil being

transported into these voids by water, localized, gradual or rapid sinking of the land surface may occur. Sinkhole collapse is a significant natural hazard. Sparse and incomplete data suggest that the average cost of karst-related damage in the US is at least $300 million per year (Weary, 2015). The actual total could be much higher given that the current statistics do not include private insurance claims and road repair costs in many states.

Due to the higher rainfall and the common presence of soluble rocks, sinkhole developments are more likely to occur in the eastern part of the US. While most of sinkholes are inherited from natural erosion process, many active sinkholes are induced or accelerated by human activities such as groundwater pumping, leaking pumping line, construction works or drainage modifications. These man-made sinkholes are often located in populated areas and are more likely to threaten public safety, private properties, and public infrastructure. The associated risks needs to be assessed for land-use planning and urban development.

Traditional sinkhole investigation methods include intrusive fieldwork such as probing, boring, drilling and trenching and non-intrusive geophysical surveys including seismic, electrical resistivity, electromagnetic conductivity, microgravity, cross-hole tomography and ground penetrating radar methods (Waltham et al. 2005). One of the major challenges in these ground-based methods is that finding small sinkholes over an extensive region is not always feasible at reasonable cost, especially in the rural areas where hydrogeologic information is limited. Satellite remote sensing data have the advantage of broad ground coverage comparing to the ground based methods. While satellite remote sensing techniques cannot replace the ground-based methods at the current stage, they can be used as a complementary data set that provide a broad survey of ground conditions and help to design the survey locations. In this study, we are working with Pennsylvania Department of Transportation to explore how these newly developed satellite remote sensing technology can be transferred to investigate sinkhole damage on highways.

3.4.2. Technology Background

Our approach is to utilize spaceborne Interferometric Synthetic Aperture Radar (InSAR) technology to detect small surface subsidence associated with karst subsidence and sinkhole collapse. InSAR is a radar imaging technique that allows us to retrieve surface deformation history with cm-level accuracy at up to meter-scale resolution. Since the launch of European Remote Sensing satellite (ERS) in 1992, high quality InSAR deformation data are available with a near global coverage. InSAR has been used successfully to study earthquakes, volcanic activities and landsides (e.g. Massonnet, 1993), as well as new earth system applications including the analysis of the atmosphere, biosphere, cryosphere, and hydrosphere (e.g. Chen et al., 2016). Stanford Radar and Remote Sensing Group has the strength in identifying new InSAR earth observation applications as well as designing computationally efficient InSAR data processing strategies for these applications. Our goal is to study to what extent the advances in InSAR technology can lead to cutting-edge scientific discoveries and

inform social decisions at all levels concerning resource and environmental management and public safety.

3.4.3. Case study 1: Bushkill Creek

3.4.3.1 Study area overview

Bushkill Creek is a 22.1-mile-long tributary of the Delaware River in eastern Pennsylvania. The geologic characters around Bushkill Creek areas include the Epler and Jacksonburg Formations, which are intensely folded and faulted with numerous joints and fractures. Weathering of these deformed units frequently lead to karst subsidence and sinkhole collapse. In October 2000, a cluster of new sinkholes started to develop around a small rural community beside the Bushkill creek near a limestone quarry (Figure 1). The quarry floor is about 50 m below the water table and it has been pumping at a mean rate of 2 m^3/s to stay dry. It would seem reasonable to ascribe the cone of depression due to the quarry dewatering process clearly has accelerated sinkhole development. These sinkholes caused damage in road bridges, railway tracks as well as private properties. Remedial action was delayed due to the lack of local hydrogeologic information. At a cost of 6 million, the Pennsylvania DoT replaced the bridge, which was damaged again in 2004 by newly developed sinkholes. Here we aim to use recent RASARSAT-2 imagery to monitor recent sinkhole related subsidence (2015-2016) in this area and explore how we can use these remote sensing data to better understand the local hydrogeology for land-use planning.

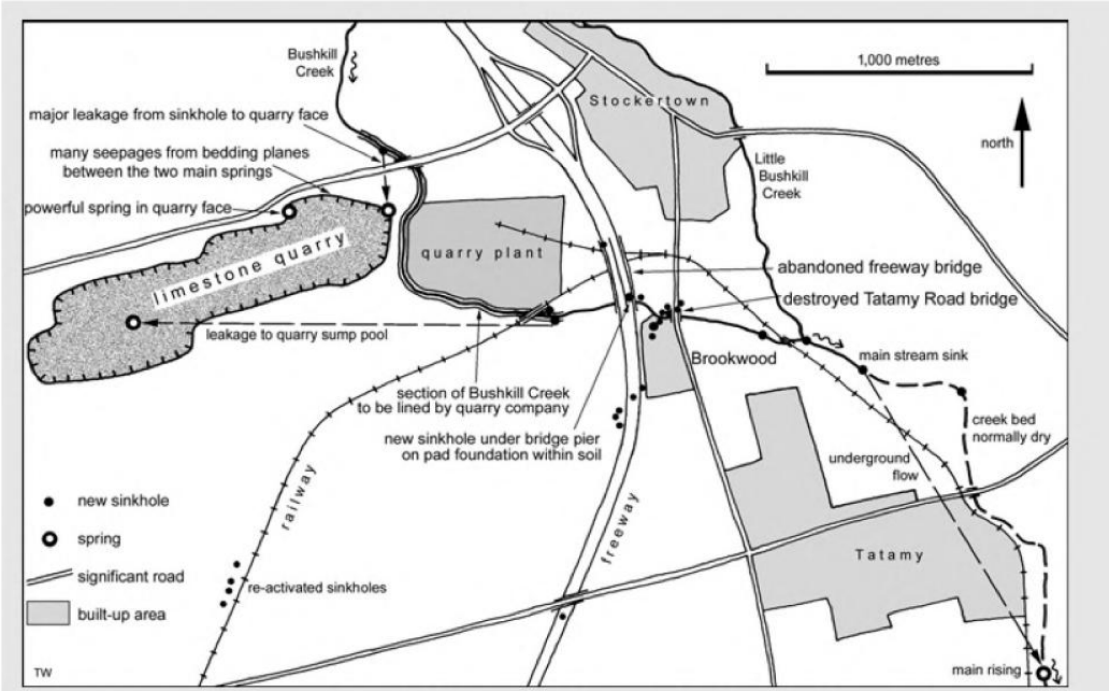

Figure 1. Outline map of the recent sinkholes and related subsidence features in the Bushkill Creek area, Pennsylvania; there are many other smaller and/or ephemeral sinkholes along the entire length of the creek covered by this map. (Waltham et al., 2005)

3.4.3.2 InSAR data processing and results

We collected 17 C-band RADARSAT-2 scenes over Bushkill creek acquired between June 11, 2015 and July 23, 2016 with a temporal resolution of 24 days. Figure 2 shows a map of Bushkill Creek area. The white square outlines the RADARSAT-2 data coverage and the red square outlines the region shown in Figure 1. Yellow lines illustrate major highways and roads, black lines illustrate railways and light blue lines illustrate local streams including Bushkill Creek.

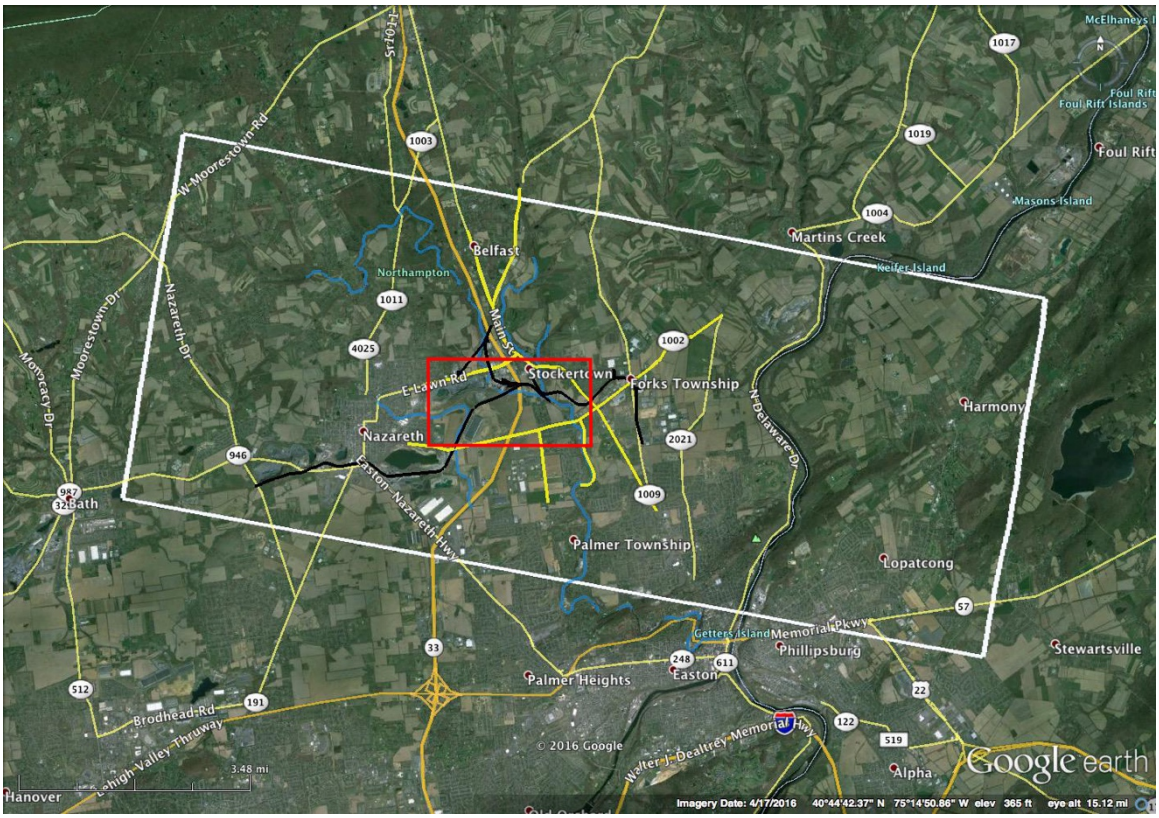

Figure 2. A map of Bushkill Creek area. The white square outlines the RADARSAT-2 data coverage and the red square outlines the region shown in Figure 1. Yellow lines illustrate major highways and roads, black lines illustrate railways and light blue lines illustrate local streams in the area of interest.

We processed all SAR scenes using a motion-compensation imaging radar processor developed at the Stanford radar interferometry group (Zebker et al., 2010) and generated 136 interferograms. We removed the topographic phase using the SRTM 3-arcsec digital-elevation database. Note that InSAR data quality is often degraded over vegetated areas due to changes in surface scattering properties, known as decorrelation artifacts. To address this challenge, we identified the persistent scatterers (PS), those InSAR pixels at which surface scattering properties do not vary much with time using a maximum likelihood estimator (Agram, 2010). Figure 3 shows the selected PS pixels over Bushkill Creek area. As we can see, the roads, railways and buildings are often identified as PS and therefore we can recover high quality InSAR deformation measurements at these targeted points. We further applied an adaptive interpolation filter between persistent scatterer (PS) pixels (Chen et al., 2015) in order to accurately unwrap the interferograms using SNAPHU and a minimum-cost flow algorithm (Chen et al., 2001). Some of the interferograms we studied contain long-wavelength phase ramps across the image. To accentuate local changes in deformation, these ramps were removed via a flattening process.

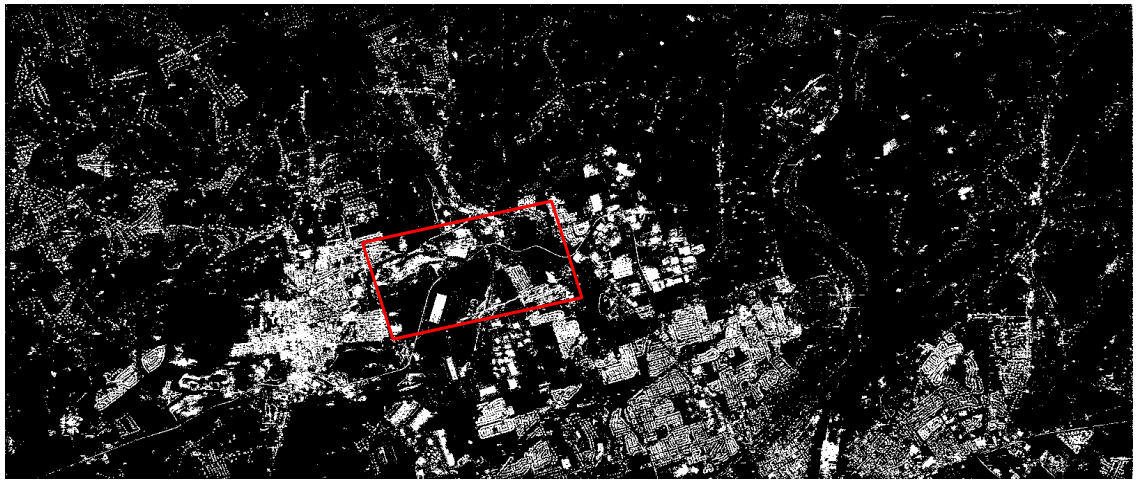

Figure 3. Identified PS pixels marked in white over Bushkill Creek area. The red box corresponds to the region in Figure 1.

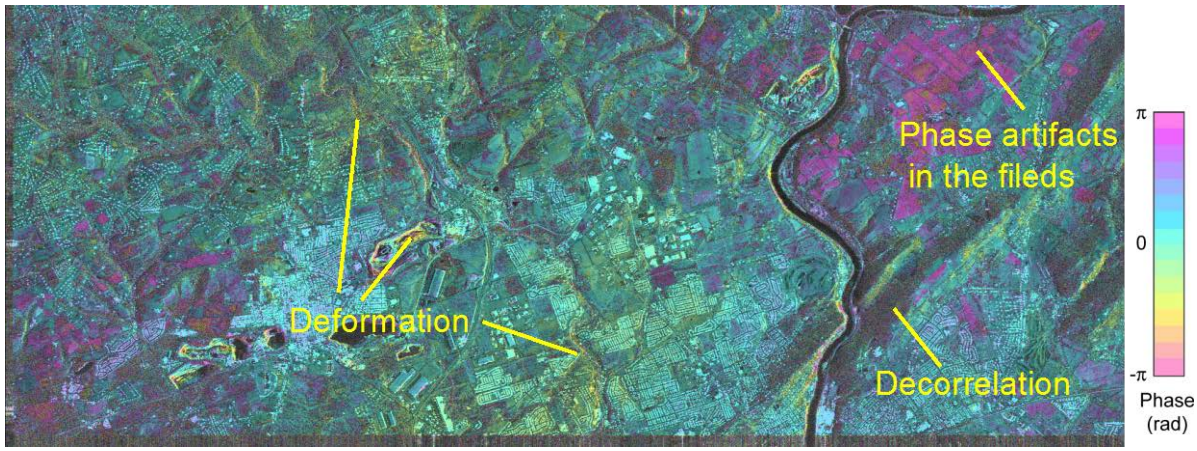

Figure 4. A sample interferogram that spans Jan. 13, 2016 and Feb. 6, 2016.

As an example, Figure 4 shows a RADARSAT-2 interferogram that spans Jan. 13, 2016 and Feb. 6, 2016. Here deformation signals are measured in the radar Line-of-Sight (LOS) direction and a phase cycle of 2π here corresponds to 2.75 cm LOS deformation. A positive LOS phase measurement between a pixel of interest and the reference pixel means that this pixel is moving away from the radar satellite with respect to the reference pixel. We observe deformation signatures near the quarry shown in Figure 1 as well as along the Bushkill Creek and at nearby towns where sinkhole development was previously reported. We also observe decorrelation or phase artifacts at the non-PS pixels due to the change in surface scattering properties. For the rest of the study, we applied a mask to exclude these non-PS pixels and limit our analysis only to the PS pixels such as buildings, roads and railways.

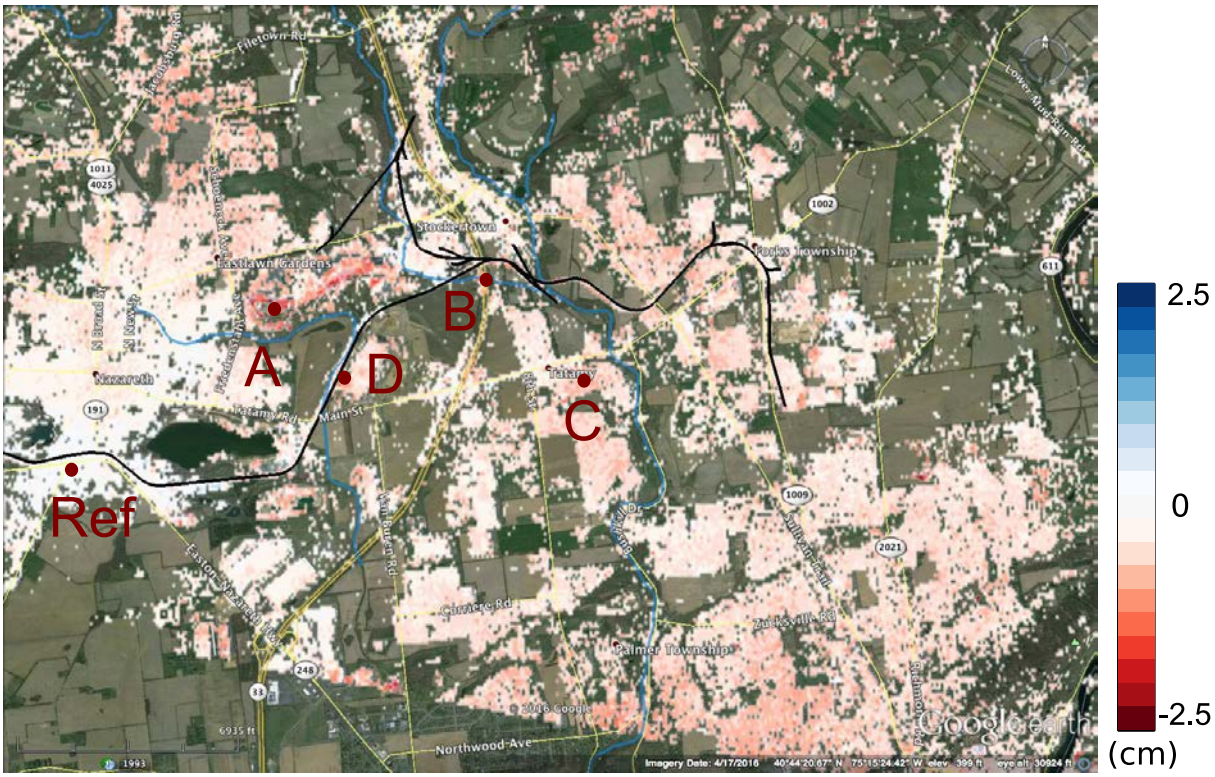

Figure 5. The total subsidence over the study area between June 11, 2015 and July 23, 2016 as derived from a linear deformation model.

To integrate all 136 interferograms and reduce noise due to tropospheric delays, we applied an SBAS time series analysis (Berardino et al., 2002) to extract surface deformation time series at each targeted PS pixel. Assuming there is little horizontal motion over the study area, we converted InSAR LOS deformation to vertical deformation. Figure 5 shows the total subsidence over the study area between June 11, 2015 and July 23, 2016 as derived from a linear deformation model. Note that InSAR measures relative motion between pixels and the observed subsidence here is relative to a reference point south of Nazareth as marked in Figure 5. A maximum subsidence ~2.5 cm can be observed at the limestone quarry (point A), near which the cluster of sinkholes were rapidly developed in the early to mid-2000s as shown in Figure 1. In general, the high subsidence regions mapped by InSAR are well correlated with areas where recent sinkhole development was reported, such as along Bushkill Creek, along Route 33, along the railway tracks and at towns near the quarry. This result indicates that the potential risk of sinkhole damage over the study area remains high in the near future. We marked another three points of interest in Figure 5: Point B is located at a Route 33 Bridge over Bushkill Creek, Point C is located at a town Tatamy and Point D is located at the railway near the quarry. All three locations suffered from serious sinkhole damage in the early to mid-2000s. Figure 6 illustrates InSAR derived vertical deformation history between June 2015 and July 2016 at Points A-D as marked in

Figure 5. At the limestone quarry (Point A), we observed periodic surface subsidence and rebound due to pumping activities. This frequent de-watering process is required for the limestone quarry mining operations. It is well known that the resulting deep cone depression can induce or accelerate sinkholes in the surrounding areas. This is consistent with InSAR time series at B, C and D, which all suggest that the ground is sinking and new sinkholes might be developing in the areas.

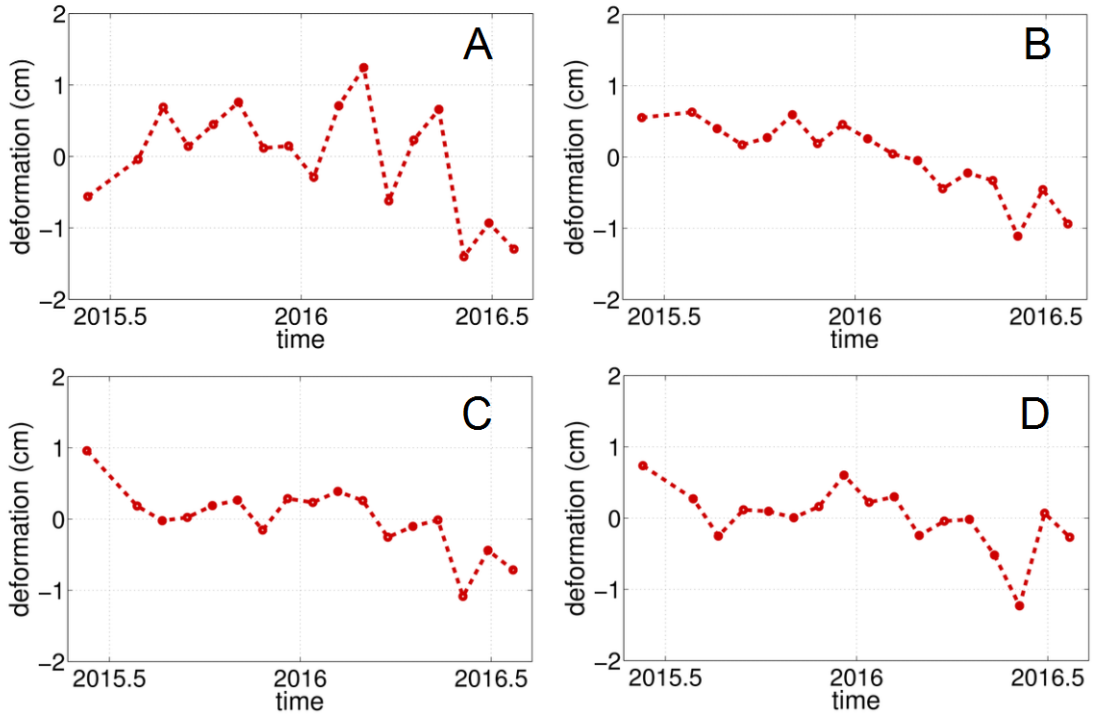

Figure 6. InSAR derived vertical deformation history between June 2015 and July 2016 at Points A-D as marked in Figure 5.

3.4.4. Case study 2: Lewistown Narrows

3.4.4.1 Study area overview

The Lewistown Narrows is an 8-mile stretch of highway conveying State Routes 22/322 through the Juniata River water gap in Shade Mountain, Central PA. As the main road between the State College area and Harrisburg, this winding road has been the site of numerous fatalities over the years. In December 2007, a major construction was completed by Penn. DoT to convert the old two-lane highway to a divided, limited-access four-lane highway. The talus rock (loose rock) formation, the underlying layer of slippery clay and the slope of Shade Mountain make it difficult to maintain the roadway stability. To address this challenge, the Lewistown Narrows project include 16

structures totaling more than four miles of retaining walls, including a two-mile-long mechanically stabilized earth (MSE) wall to withstand lateral earth and water pressures and preserve the shape of the roadway. Maintaining the stability of this road is an continous effort and here we aim to use recent RASARSAT-2 imagery to monitor the ground motions of the Lewistown Narrows during 2015 to 2016.

3.4.4.2 InSAR data processing and results

We collected 18 C-band RADARSAT-2 scenes over Lewistown area acquired between June 03, 2015 and August 08, 2016 with a temporal resolution of 24 days. Figure 7 shows a map of Lewistown area. The white square outlines the RADARSAT-2 data coverage and yellow lines illustrate major highways and roads. The Lewistown Narrows is marked as Route 22 in dark yellow.

Figure 7. A map of Lewistown area. The white square outlines the RADARSAT-2 data coverage and yellow lines illustrate major highways and roads. The Lewistown Narrows is marked as Route 22 in dark yellow.

We processed all SAR scenes in the same way as described in Section 3. Note that we excluded the SAR scene acquired on August 14, 2015 because all interferograms generated using this SAR image have spatial baselines beyond critical baseline and no coherent phase measurements can be recovered. Figure 8 shows the identified PS pixels over Lewistown area. Because of the dense vegetation in the study area, there are very few PS pixels outside Lewistown except along roads and railways. Nonetheless, high quality InSAR phase measurements can be obtained along the Lewistown Narrows for the purpose of this project. We applied an adaptive interpolation filter between PS pixels (Chen et al., 2015) in order to accurately unwrap the interferograms using SNAPHU and a minimum-cost flow algorithm (Chen et al., 2001). Long-wavelength phase ramps were removed after phase unwrapping. Due to the low PS pixel density, phase unwrapping is not successful for a small portion of the interferograms despite the implementation of the PS interpolation filter. We analyzed all unwrapped interferograms and only include 101 out of 136 interferograms with minimal phase unwrapping errors in the final analysis.

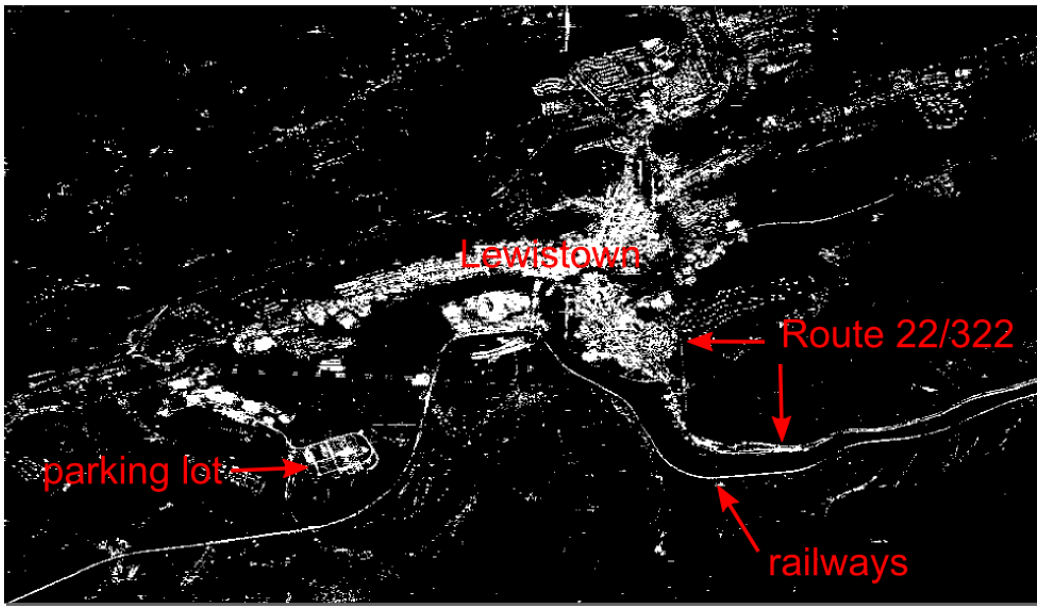

Figure 8. Identified PS pixels marked in white over Lewistown area.

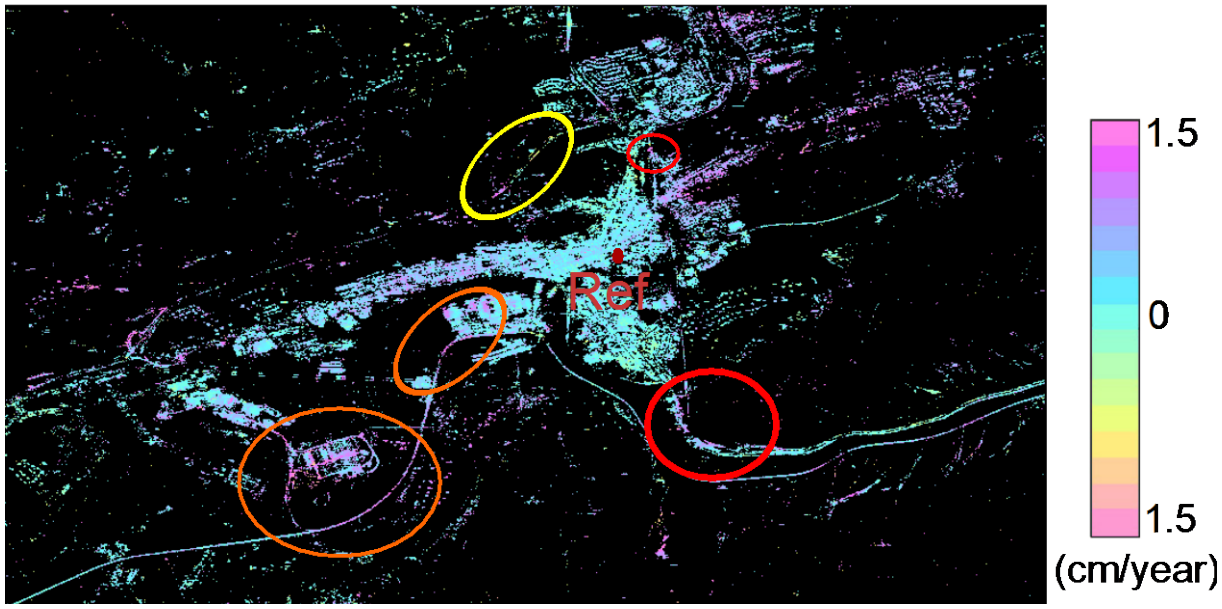

Figure 9. The annual LOS deformation rate at PS pixels over Lewistown area as derived from a 7-interferogram stack. The deformation is measured with respect to the reference point in Lewistown as marked in the figure. We identify several areas with relative high deformation rates (~1 cm/year) along the Lewistown Narrows in red, along the Route 522 in yellow and along the local railways and a nearby parking lot in orange.

Given that both vertical and horizontal deformation might occur in the hilly terrain, we present the surface deformation in the LOS direction to map areas that are less stable. While this is sufficient for the purpose of this study, vertical and horizontal motion on the same order of the LOS motion can be separated if SAR data from multiple imaging geometries are available. To reduce noise due to tropospheric delays, we calculated the ground LOS deformation rate at each PS pixel by averaging 7 independent 216-day interferograms generated from 14 SAR scenes. The inferred annual LOS deformation rate relative to a reference point in Lewistown is shown in Figure 9. An SBAS analysis assuming a linear deformation model yields similar results. We observe that along most section of the Lewiston Narrows (Route 22/322), there is little surface deformation occurred between 2015-2016. This indicates that the engineering works done in the 2007 Lewistown Narrows met the expectation. We identify several areas with relative high deformation rates (~1 cm/year) along the Lewistown Narrows in red, along the Route 522 in yellow and along the local railways and a nearby parking lot in orange. These less stable sections are more likely to occur at the turning point along roads and railways, which may cause local strain accumulation and future damage on the roads and railways.

The above data were examined by Prof. Lakshmi, his response and discussion can be summarized here. He generated a report on the effects of soil moisture on infrastructure largely through reference to literature, his specific comments were comparing and combining InSAR backscatter with remotely sensed and in-situ soil moisture.

The InSAR sensor provides backscatter at high spatial resolution on large spatial scales. Backscatter at L and C bands is responsive to surface dielectric constant (soil moisture, vegetation) and is modified by surface roughness (soil surface and vegetation) (Dobson and Ulaby, 1986). Early work using tower and truck mounted radar systems carried out observations on bare soil and vegetated fields (refs) to derive simple regression relationships between backscatter and soil moisture dependent on the type of the surface. Field observations have also been used to derive soil moisture from satellite sensors (Dobson and Ulaby 1986). The development of complete scattering models such as IEM (Fung et al.1992) have led to better interpretation of the observations (Panicera et al. 2014).

However, to determine soil moisture from InSAR or other active sensors an innovative change detection technique can be used (Du et al. 2000, Narayan et al. 2006). This method assumes that the difference between two consecutive backscatter observations is a function of soil moisture change independent of vegetation. However, this is restricted to backscatter observation pairs that are a few (1-4) days apart when the vegetation characteristics can be assumed to be constant.

Routine observations of soil moisture are available from standard networks –United States Department of Agriculture – Agricultural Research Service Soil Climate Analysis (USDA-ARS SCAN) network provides hourly soil moisture at several sites in United States and around 2-3 sites in each state (http://www.wcc.nrcs.usda.gov/scan/)

With the development of Unmanned Aerial Vehicles (UAV), there is a development of soil sensors that can be used on demand (Capolupo et al. 2015). However, UAVs are limited by the weight of the payload and power requirements and this limits the use of active radars that are heavy and need a lot of power.

There are a number of indirect measurements of soil moisture or wetness of the surface. Firstly, knowledge of the past precipitation is a good indicator of soil wetness. The Antecedent Precipitation Index (API) is a weighted sum of past rainfall – higher API indicates higher soil moisture (Fedora and Beschta, 1989). Secondly the change in the surface temperature (afternoon minus morning surface temperature) – higher soil moisture is associated with smaller value of surface temperature change as water has greater thermal inertia than dry soil.

THIS PAGE INTENTIONALLY LEFT BLANK

4 INSAR ANALYSIS METHODS

This section provides an overview of the methods used during the project to process data from the four study sites. These include:

1. MDA's HDS-InSAR method which was used to generate deformation estimates for all four study sites.
2. 2D-decomposition of combined ascending and descending pass direction data to derive vertical and east-west deformation components. This was applied to both the Seattle and Geysers datasets.
3. Layover and shadow prediction using high quality DEM information. This was applied to the Seattle dataset in order to predict locations in the SAR imagery affected by layover and/or shadow.

4.1 HDS-InSAR

HDS-InSAR was used to process the RADARSAT-2 data stacks and generate multi-temporal surface deformation estimates along the line-of-sight (LOS) for each data stack. HDS-InSAR uses adaptive multi-looking over local neighbourhoods with statistically similar amplitude distributions in order to supress noise over distributed targets while preserving point like targets. The adaptive filtering improves or maintains temporal coherence for multiple target classes such as buildings, roads and sparsely vegetated terrain during InSAR processing. This method is therefore well suited for the four project sites which include urban, sub-urban and natural terrain areas containing a variety of infrastructure types. Fig. 4-1 shows the HDS-InSAR processing steps. These steps are designed to:

1. supress phase noise through combined adaptive filtering and phase modeling to,
2. identify coherent targets (i.e. those with sufficient phase quality after noise suppression and,
3. estimate the deformation time history for each coherent target.

The resulting output of the processing are a series of cumulative deformation maps with low-coherence targets omitted. These maps may be viewed either spatially as two dimensional maps, or temporally as a set of one dimensional deformation plots (one per coherent target).

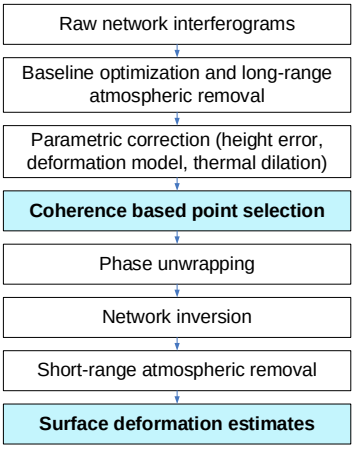

Figure 4-1 HDS-InSAR Processing Steps

4.2 2D Decomposition

Both ascending and descending pass direction datasets were obtained for the Seattle and Cobb datasets. This provides the opportunity to decompose the results for these sites into vertical and horizontal deformation components. This section summarizes this concept and provides an example of its use for a symmetric case of combined vertical + horizontal deformation.

Two data stacks from opposing satellite pass directions may be processed to derive a corresponding pair of line-of-sight (LOS) multi-temporal deformation estimates. Each LOS measurement corresponds to the projection of the true deformation vector along the sensor LOS. The two LOS vectors together form a basis over a 2D plane and therefore it is possible to compute orthogonal deformation components within this plane. Deformation components orthogonal to this plane are orthogonal to both stack LOS vectors and are therefore not observable by the paired measurements. As such it is not possible to fully recover the 4D deformation vector given a pair of measurements. However it is straightforward to solve for the specific solution with a minimum norm that corresponds to assigning a zero to the out-of-plane component, which is the approach taken in this project.

With the measurement geometry of opposing RADARSAT-2 pass directions the out-of-plane direction corresponds approximately to the north-south axis and therefore only vertical and east-west direction components are reported. It should be noted that since the out-of-plane component is not exactly aligned with the north-south axis, the estimated vertical and east-west components are biased by the out-of-plane component to a small degree.

A simulation is presented to demonstrate the utility of the 2D decomposition at estimating the vertical and east-west component of a circularly symmetric deformation field and to show the effect of measurement bias. Fig. 4-2(A) shows a simulated circularly symmetric deformation field with 0.5*(1+cos(r)) radial profile and with horizontal deformation proportional to the vector spatial gradient of the vertical component. The LOS measurements corresponding to the geometry of the two image stacks used in this study are shown in Fig. 4-2(B). Note the east-west shift in the location of the peak LOS deformation between the two geometries.

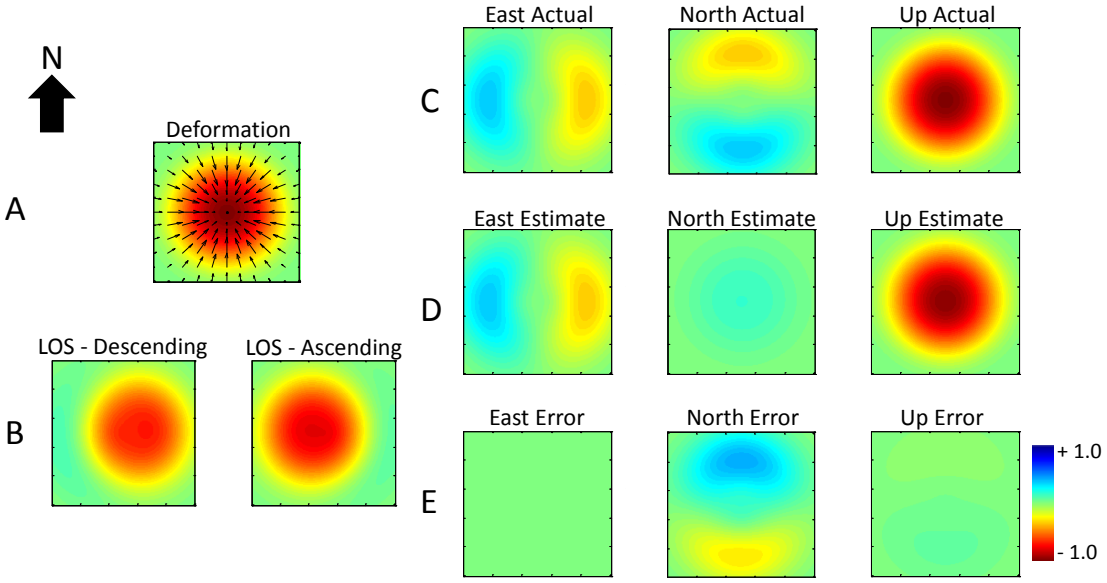

Figure 4-2 (a) Simulated deformation field. Colour depicts vertical deformation magnitude, arrows depict horizontal deformation magnitude and direction. (b) Corresponding LOS components for the two image stack geometries. (c) (d) and (e) 2D decomposition simulation results showing actual deformation, estimated deformation and errors.

Fig. 4-2(c), (d) and (e) shows the actual, estimated and bias components resulting from applying the 2D decomposition to the simulated LOS measurements. Examining the bias components shows that the west direction bias is negligible, the up component is small and coupled to the actual north component and the north component bias comprises most of the actual north component. This simulation result validates the 2D decomposition in the case when the north component is of equal or lesser magnitude than the up and east components.

4.3 Improved Identification of Layover/Shadow Areas

The visibility of the terrain in different portions of a radar scene can be affected by the orientation of the radar line-of-sight (LOS) with respect to the local incidence angle. These differences in slant range and ground range produce geometrical distortions known as shadow and layover. Shadow occurs when an object blocks the radar energy from reaching a point; therefore the radar is not able to illuminate this region (Fig. 4-3). Layover occurs when radar scatterers have different physical positions but have the same distance to the sensor and are in the same Doppler plane, and therefore appear collocated in the radar geometry. The layover/shadow geometry is depicted in Fig. 4-3. These effects are pronounced in urban centers since the contributions from building facades, rooftops and surrounding ground-level elements may overlap which makes interpretation of SAR images difficult. For InSAR processing in urban areas it is helpful to know the location of these effects a priori to obtain better phase estimations and avoid incorrect interpretation of deformation.

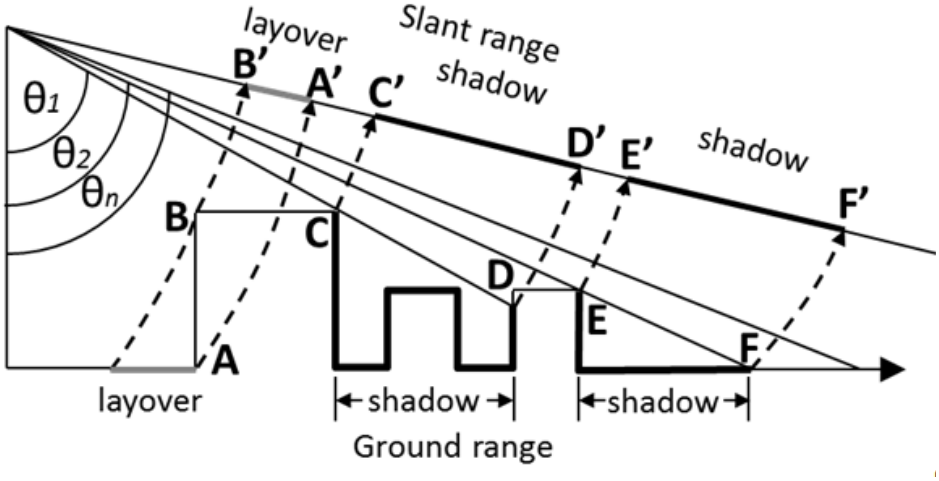

Figure 4-3 Shadow and layover effects in SAR imagery in urban areas.

A shadow and layover simulator was developed during this project to estimate the areas affected by these geometrical distortions. The primary motivation for this work is the Seattle area of interest which includes many tall buildings with significant areas in layover and/or shadow. Shadow and layover masks are created to improve point selection during the InSAR processing and to prevent ambiguities during geocoding of results from the radar geometry to geodetic coordinates. The input to the simulator consists of a DEM in geodetic coordinates containing the building height information. A lookup table of ground range and azimuth coordinates is estimated using the WGS84 ellipsoid with mean average elevation of the DEM. Then the lookup table is used to project the DEM into ground range and azimuth coordinate system and estimate the shadow and layover mask along the range direction. To estimate the shadow and layover mask it is necessary to first derive a local incidence angle map. The areas of true shadow are the locations where the angle between the local incidence angle and the satellite look angle is greater than 90°. Then, starting from this location, we estimate if

this object produces a shadow in the neighbor pixels along the range direction. The areas of true layover are the locations where the angle between the local incidence angle and the satellite velocity vector is greater than 90°.

First, we developed a prototype of the shadow/layover simulator and used a synthetic DEM to verify that the regions of true shadow/layover were properly identified based on the local incidence angle. Also we wanted to verify if shadows were properly propagated along the range direction. Fig. 4-4 shows an example of a synthetic DEM and the estimated shadows using two different incidence angles and two different look directions (west-east and east-west). As expected, shallow incidence angles produce large regions of shadow compared to steeper incidence angles. Also the synthetic results show that the propagation of shadow is correct over neighborhood buildings with different heights.

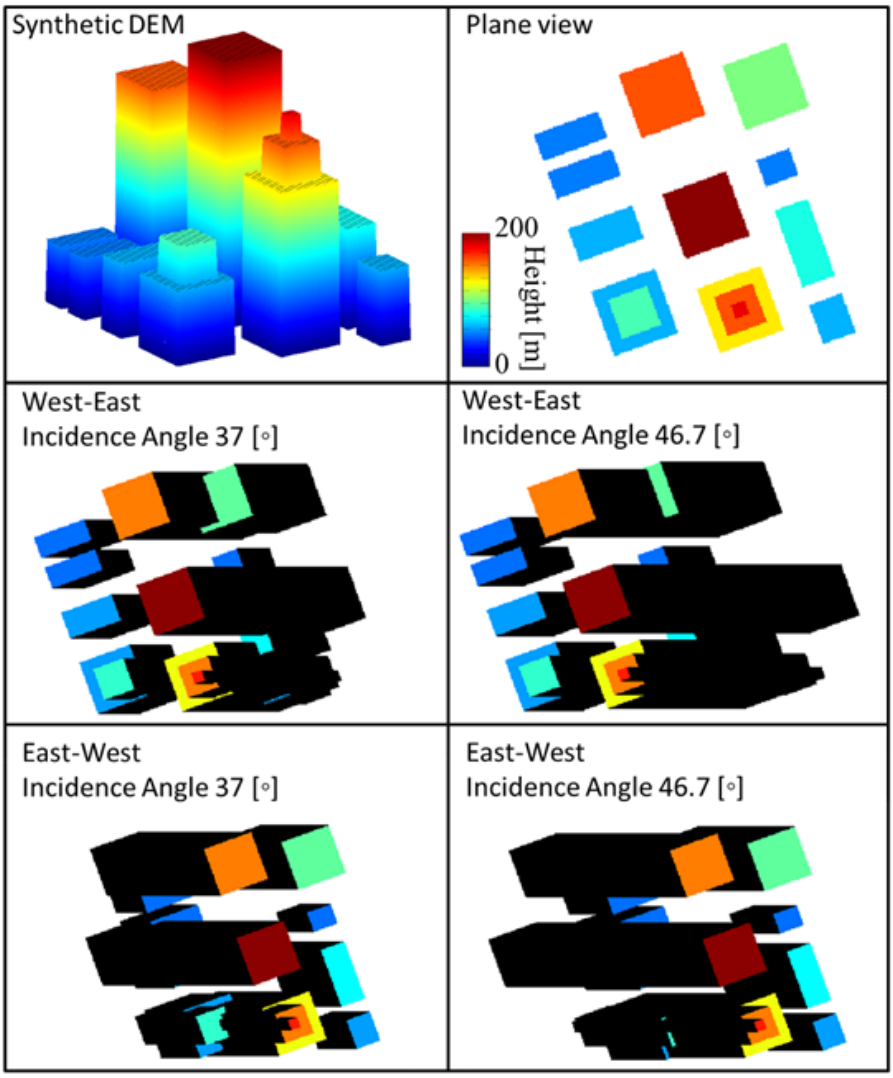

Figure 4-4 Shadow and layover effects in over a synthetic DEM representing an urban area.

The shadow/layover algorithm was applied to the refined Seattle DEM described in Section 5.1.2. Fig. 4-5 shows the estimated areas of shadow in geographic coordinates for the descending track SLA24 and the ascending track SLA9 covering downtown Seattle. Shadows for SLA24 are southeast-northwest oriented, while for SLA9 the shadows orientation are southwest-northeast. Due to the differences of the incidence angle, shadows are larger for SLA24 (46.7°) than SLA9 (47°). Results also show that buildings roofs with heights above the shadow zone are not masked out. The accuracy to which the shadow is estimated strongly depends on the accuracy of the heights provided in the DEM. For areas without building heights the simulator estimates the shadow and layover mask using the DEM without building heights. In Fig. 4-6 we show an example of the effects of layover over the descending passes. Steep incidence angles produce large regions of layover compared to shallow incidence angles.

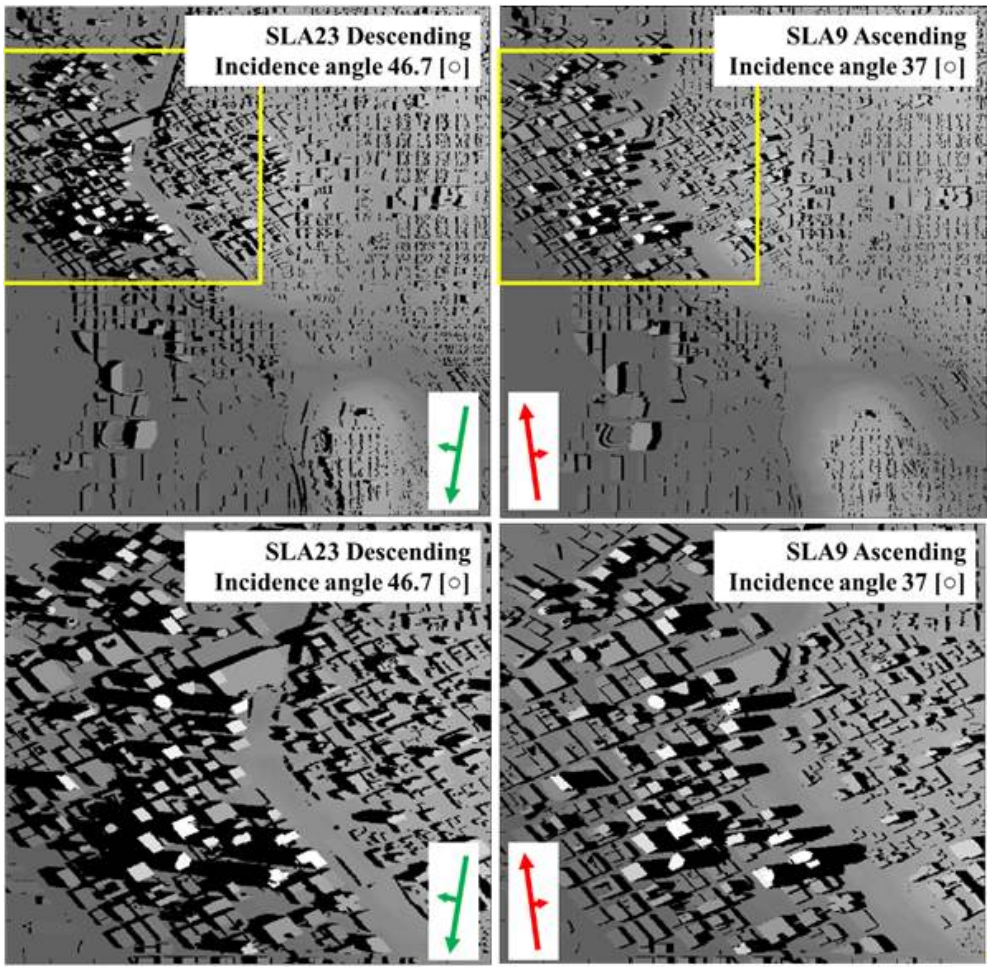

Figure 4-5 Top panels: Simulated shadows over Seattle downtown area for the descending and ascending geometries. Bottom panels: Zoom of the area with the highest buildings.

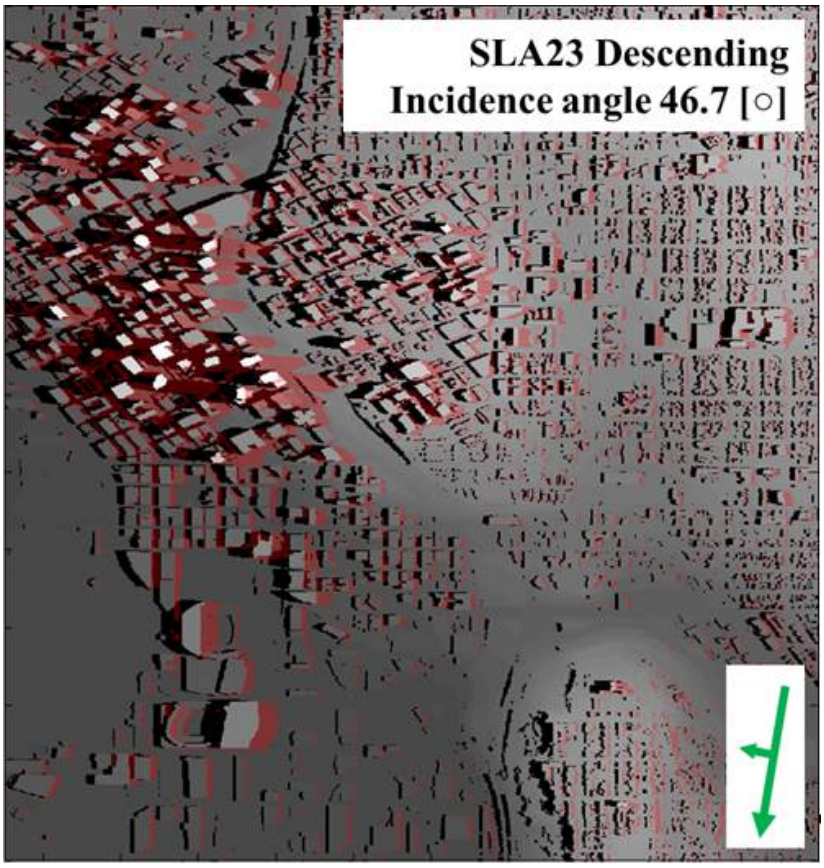

Figure 4-6 Simulated shadows (black) and layover (red) over Seattle downtown area for the descending pass SLA24.

The shadow/layover mask may be used during subsequent InSAR processing to improve results (e.g. improved geocoding of the line-of-sight deformation maps prior to 2D deformation estimation).

The simulation currently assumes the zero Doppler imaging condition and neglects both diffraction effects and the fact that ground targets are illuminated over a finite synthetic aperture rather than just the instantaneous zero Doppler point.

THIS PAGE INTENTIONALLY LEFT BLANK

5 INSAR ANALYSIS RESULTS

This project includes InSAR based monitoring of four study sites identified from three state DOTs:

1. SR99 Tunneling project (Seattle, Washington)
2. Lewistown Narrows project Mechanically Stabilized Earth (MSE) retaining walls (Lewistown, Pennsylvania)
3. Bushkill Creek area limestone karst sinkholes (Northampton County, Pennsylvania)
4. The Geysers geothermal field (California)

For the Seattle and Geysers sites both ascending and descending pass direction data stacks were processed allowing for decomposition of the two LOS deformation estimates into vertical and east-west components. For the Lewistown Narrows and Bushkill Creek sites only single direction datasets were processed and therefore results for these sites are presented as LOS deformations only.

5.1 Seattle, Washington

This section presents results for InSAR based deformation monitoring of the Washington State Department of Transportation (WSDOT) SR 99 Bored Tunnel Project currently underway in Seattle. The goal of this construction project is to replace an existing above surface elevated road viaduct through downtown Seattle with a 57 [ft] diameter, 2 mile long bored tunnel roadway. Figure 5-1 shows a map of the planned tunnel route and the approximate tunneling progress as of September 2016.

Boring was initiated in July 2014 and progressed 0.2 miles by December 2014 at which time the boring machine encountered a mechanical failure which required the construction of a vertical rescue shaft to initiate repairs. Construction of the 120 [ft] deep by 80 [ft] diameter shaft involved significant dewatering through wells accessing

three aquifer zones: a shallow zone, a mid-level zone and a deep zone (> 200 [ft]), extending down to glacial deposits.

The dewatering that took place is highly correlated with additional settlement in the vicinity of the rescue shaft spanning an area of roughly 1 km^2 as measured by InSAR and reported previously R-2. The settlement since the initial dewatering then stabilized and has rebounded to near pre-dewatering levels after cessation of dewatering.

Figure 5-1 Planned tunnel route showing current location of tunnel boring machine 'Bertha' (image courtesy WSDOT).

Two RADARSAT-2 Spotlight mode image stacks from opposing look directions were acquired over the project site from 6 June 2012 to 27 July 2016 at 24 day intervals per stack. This time period includes ten months prior to start of boring, the initial boring phase and the subsequent construction of the rescue shaft and associated dewatering, and finally the restart of tunnelling.

HDS-InSAR was used to process the two RADARSAT-2 data stacks to derive multi-temporal surface deformation estimates along two satellite lines-of-sight (LOS). These estimates were then decomposed into separate time resolved maps of vertical and east-west deformation.

These maps were further decomposed into a set of temporal cumulative deformation maps which divide the deformation into segments in time corresponding with significant events in the timeline of the tunnelling project. Figure 5-2 below shows the timeline of the project and marks the time periods of RADARSAT-2 data shown in the resulting deformation maps.

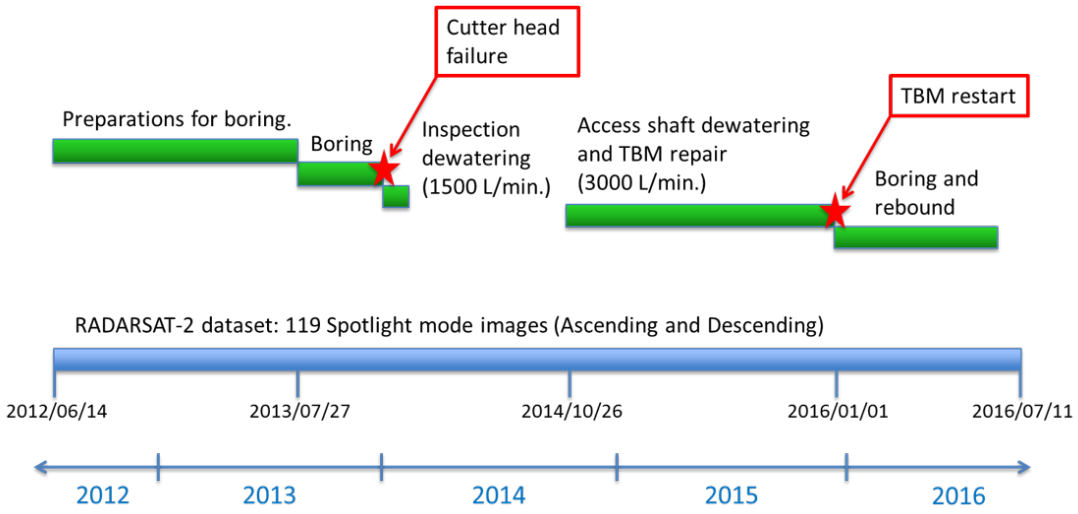

Figure 5-2 Approximate timeline of tunneling project with the time periods of interest marked.

5.1.1 SAR Data and Processing

Two RADARSAT-2 Spotlight stacks from opposing satellite pass directions were acquired in order to allow for 2D-decomposition of deformation estimates – see Table 5-1. Spotlight data have a resolution of 5.4 [ft] in slant range and 2.6 [ft] in azimuth (i.e. along satellite track) directions. These data were multi-looked during processing to produce images that have ~10 [ft] resolution in both ground range and azimuth directions. Figure 5-3 shows the ground footprints of the two stacks and the 4.4 sq. mile processed area of interest, which includes the southern 2/4 of the planned tunnel and surrounding area.

Table 5-1 Characteristics of Seattle RADARSAT-2 Stacks

	Beam Mode	
	SLA9	**SLA24**
Look Direction	Asc	Des
Centre incidence angle [°]	47.0	46.7
Ground-range resolution [ft]	8.9	7.2
Azimuth resolution [ft]	2.6	2.6
Rng x Az swath [miles]	11x5	11x5
Number of scenes	62	60
Stack Start date	Jun-2012	June-2012
Stack End date	Jul-2016	Jul-2016

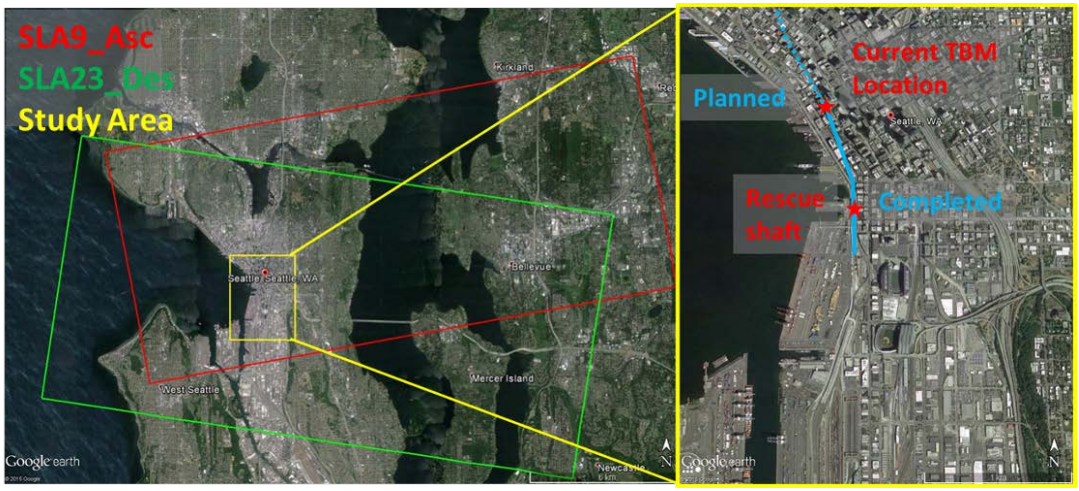

Figure 5-3 RADARSAT-2 data footprint map showing per stack ground coverage and processed study area of interest.

Additional data required for the InSAR processing include: 1) a Digital Elevation Model (DEM) for topographic phase correction and projection from radar to map coordinates. See Section 5.1.2 below for a detailed description of the refined DEM, and: 2) mean daily temperatures recorded at the Seattle–Tacoma International Airport for estimation and removal of deformation due to thermal dilation of rigid structures.

5.1.2 Refined Digital Elevation Model

The Seattle study area includes the downtown urban core of the city with a dense set of tall buildings and significant layover/shadow areas. For this reason, the Seattle DEM that was used for initial processing was refined with orthophoto derived building height data available from a Seattle municipal database. This was done to investigate the benefits of using more accurate height data in an urban environment and increase the precision of the InSAR results.

The original DEM that was used for processing was created by merging a high resolution 1/9 arc-second NED DEM with a 4 arc-second SRTM90 DEM tile to fill any missing data that was not available in the NED DEM. The NED DEM covers most of the Seattle area including the areas of interest. While the 1/9 arc-second elevation data is at a high resolution it represents only the terrain and does not contain any building height data. Below in Figure 5-4 and Figure 5-5 are renderings of the original merged DEM used for processing along with an inset showing downtown Seattle.

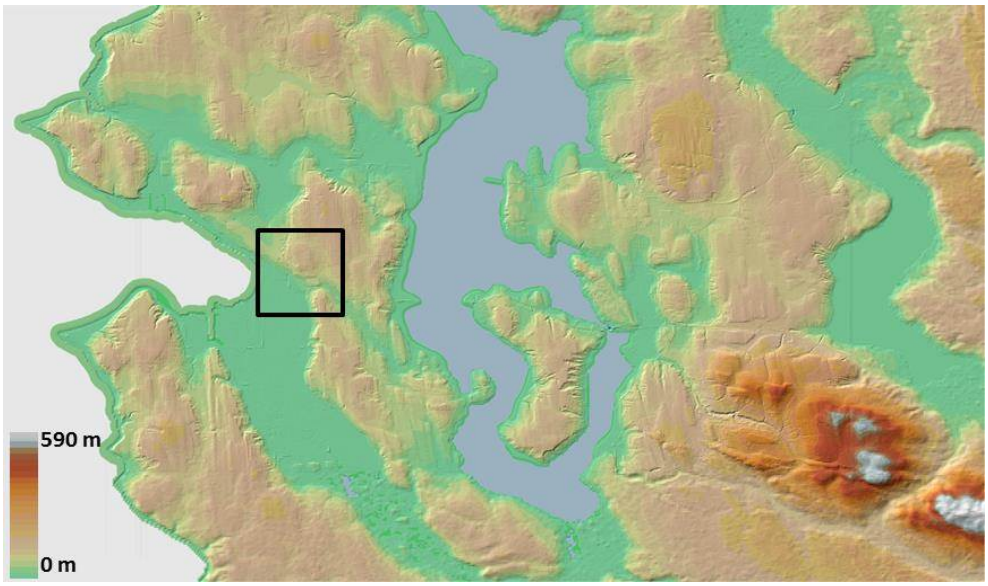

Figure 5-4 Original merged DEM containing 1/9 arc-second NED data and 4 arc-second SRTM90 data.

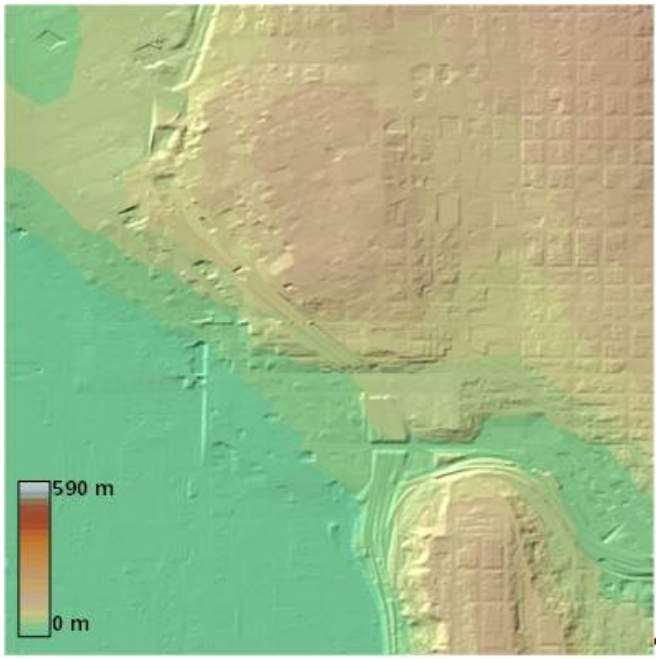

Figure 5-5 Zoom in over Seattle downtown area of original merged DEM.

The refined DEM was created by ingesting and applying building height data (derived from data acquired in 2009) obtained from www.data.seattle.gov. The shapefile consists of the polygon outline of the buildings and the peak roof height. The dataset has a NAD84 horizontal datum and a geoidal vertical datum (appearing to be Geoid 2012 Revision A although not explicitly specified). The dataset was transformed horizontally to WGS84 and vertically to the WGS84 ellipsoid by correcting for the geoid in the

dataset. The polygons were extracted from the transformed dataset and the corresponding pixels in the DEM where filled with the height value for the building.

Validation was done in an ad hoc fashion by comparing the resulting building heights in the DEM (by taking the difference between the roof and the surrounding street level height) with expected heights of houses in residential neighborhoods and also known architectural building heights for a few tall buildings in the downtown core. They were found to agree within a few meters accuracy and therefore the height data was deemed to reasonably approximation the actual building heights. It should be noted that a small fraction of buildings are missing in the shapefile and that not all building are well representing by a simple vertical extrusion of the base outline. However, in general the data provides a significant improvement in accuracy over just the SRTM/NED merged DEM. Below in Figure 5-6 and Figure 5-7 are renderings of the resulting refined DEM along with an inset over downtown Seattle emphasizing the height differences between the original DEM terrain and the actual urban infrastructure.

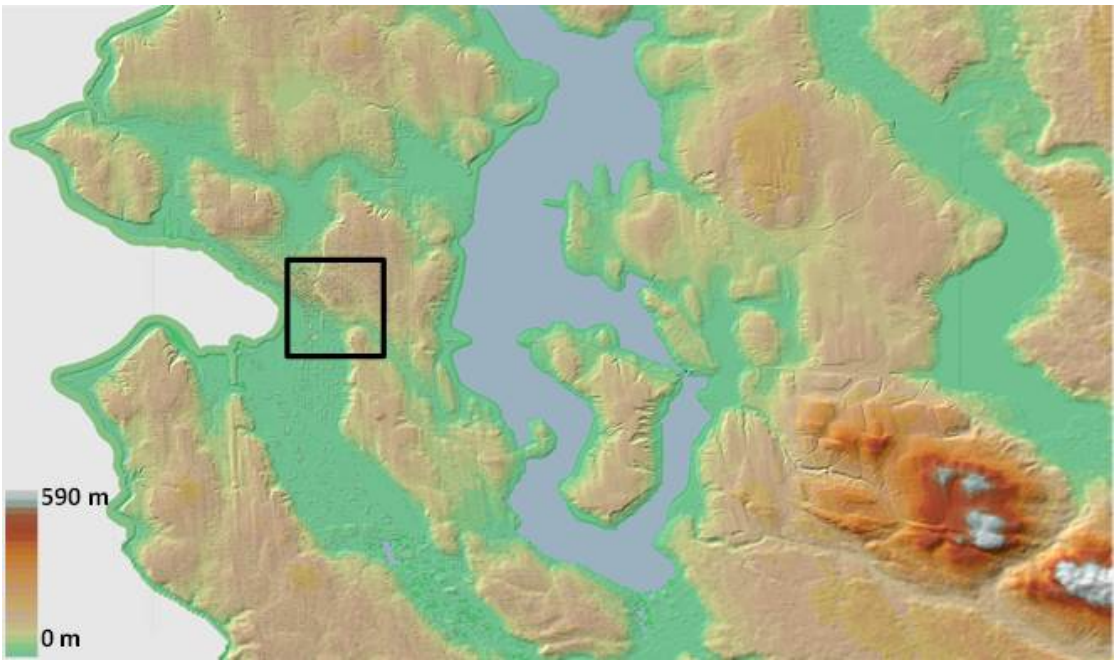

Figure 5-6 Refined DEM where the whole western side of the DEM is populated with building height data.

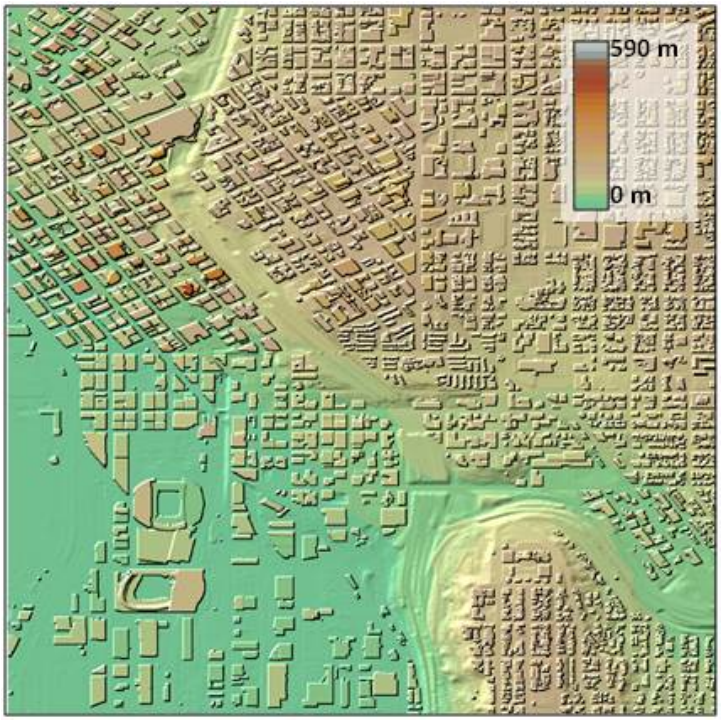

Figure 5-7 Zoom in over Seattle downtown area showing the building heights along with the original terrain data.

5.1.3 Line-of-Sight Deformation

The ascending and descending RADARSAT-2 spotlight stacks were processed with HDS-InSAR to generate multi-temporal line-of-sight (LOS) deformation estimates. Figure 5-8 shows spatial maps of cumulative deformation for the 50 month data acquisition period. Note that positive values correspond to deformation toward the sensor and negative values correspond to deformation away from the sensor. Although the majority of areas appear stable (shown in green) there are some areas near the center of the footprint and extending to the south and west which show net subsidence over the period. These areas include the Pioneer Square area and are outside the historical shoreline having been infilled since the late 1800s. Noteworthy subsidence areas include those in the vicinity of the pant-leg shaped TBM ingress zone and along the north-south oriented rail line.

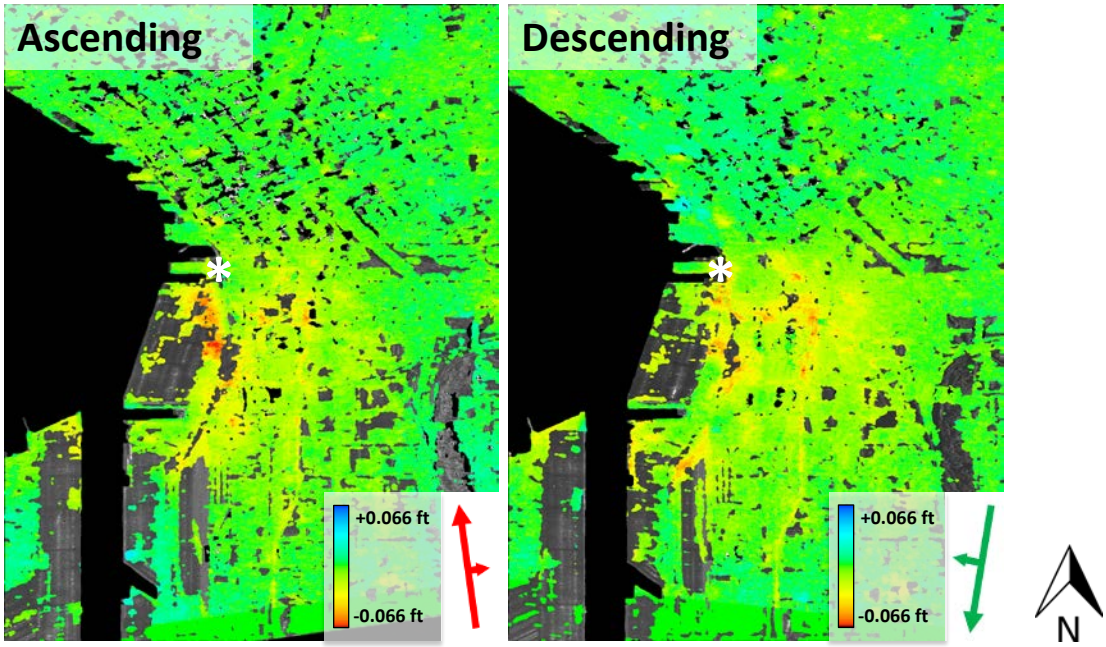

Figure 5-8 LOS cumulative deformation for the two data stacks (06/06/2012 – 27/07/2016). Location of rescue shaft is denoted with an asterisk.

5.1.4 2D Decomposed Deformation

The LOS deformation estimates were decomposed into vertical and east-west estimates as shown in Figure 5-9. Note that for the vertical case, positive values correspond to uplift and negative values correspond to subsidence. There are localized long term vertical subsidence features which have subsided ~0.07 [ft] over the monitoring period along with a wider scale net subsidence of ~0.015 [ft] which may be related to incomplete dewatering rebound. For the east-west case, positive (blue) values correspond to eastward motion and negative (yellow/red) values correspond to westward motion. Similarly the east-west component map shows localized pockets of deformation superimposed on a weak wider scale horizontal dilation also likely due to incomplete rebound of dewatering induced subsidence.

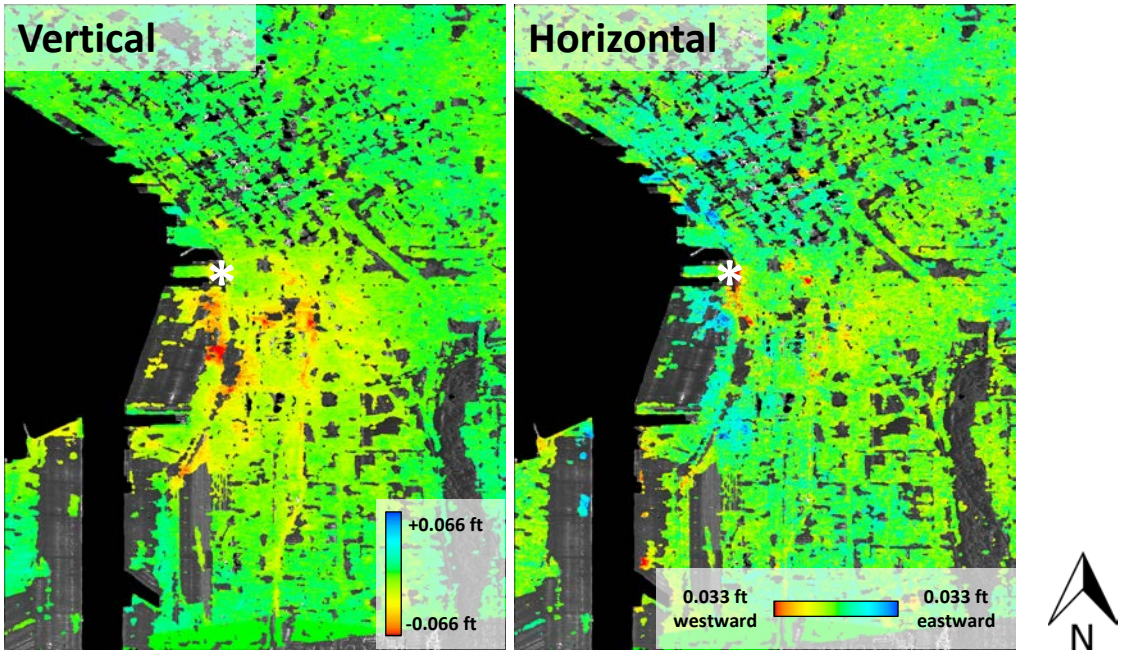

Figure 5-9 2D cumulative deformation (06/06/2012 – 27/07/2016). Location of rescue shaft is denoted with an asterisk.

5.1.5 Temporal Cumulative Deformation Periods

The deformation time series was broken down into a set of maps corresponding to the periods of interest in the construction timeline. There are four time periods shown below:

1. From start of construction to the start of tunnel boring
2. From the start of boring and the initial dewatering up to the major dewatering event
3. The period of major dewatering up to tunneling restart
4. The tunneling restart to the end of available data processed

Figure 5-10 shows the pre-dewatering estimated cumulative deformation for both the vertical and east-west cases. Some subsidence is visible in the area south of the rescue shaft which corresponds to the excavation area for TBM ingress and also the 0.2 miles of completed boring route, along with the north-south oriented rail line to the south-east of the rescue shaft location. These patterns are similar to those observed for the four year cumulative map but with reduced cumulative magnitude due to the shorter one year time span.

The east-west deformation map shows the deformation is predominately eastward. An area along the western side of the TBM ingress site shows eastward deformation of ~0.015 [ft].

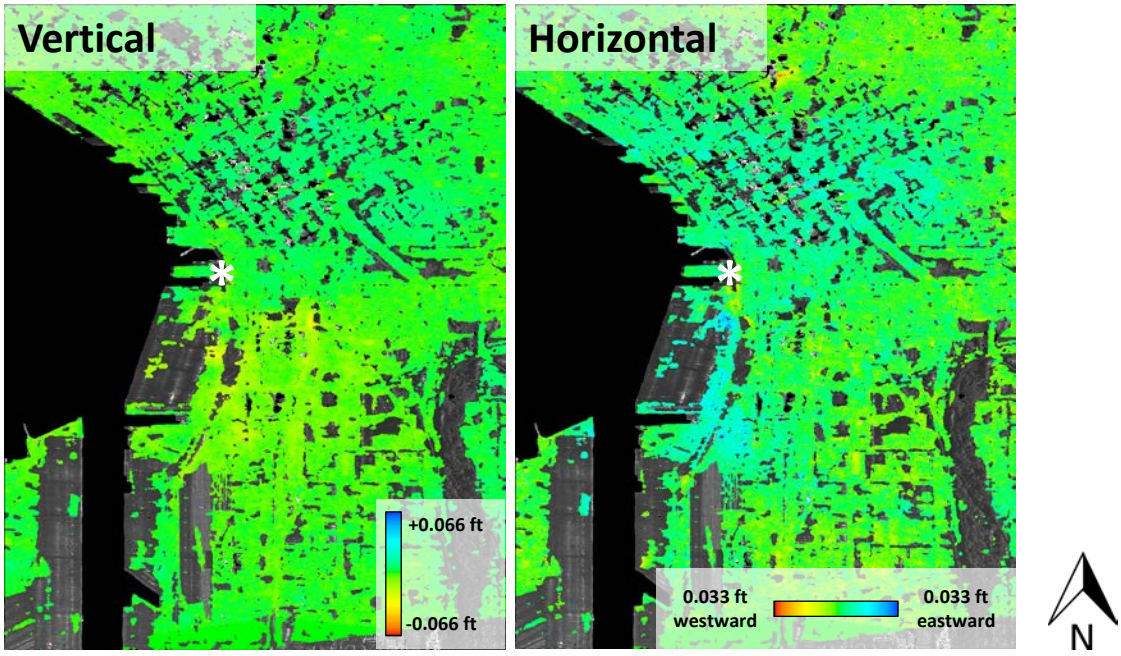

Figure 5-10 Pre-boring cumulative deformation maps (06/06/2012 – 27/07/2014). Location of rescue shaft is denoted with an asterisk.

The period corresponding to the tunnel boring, cutter head failure and initial dewatering is shown below in Figure 5-11. The majority of deformation is correlated with the initial dewatering and shows the expected deformation signal in both vertical and east-west directions corresponding to a subsidence bowl.

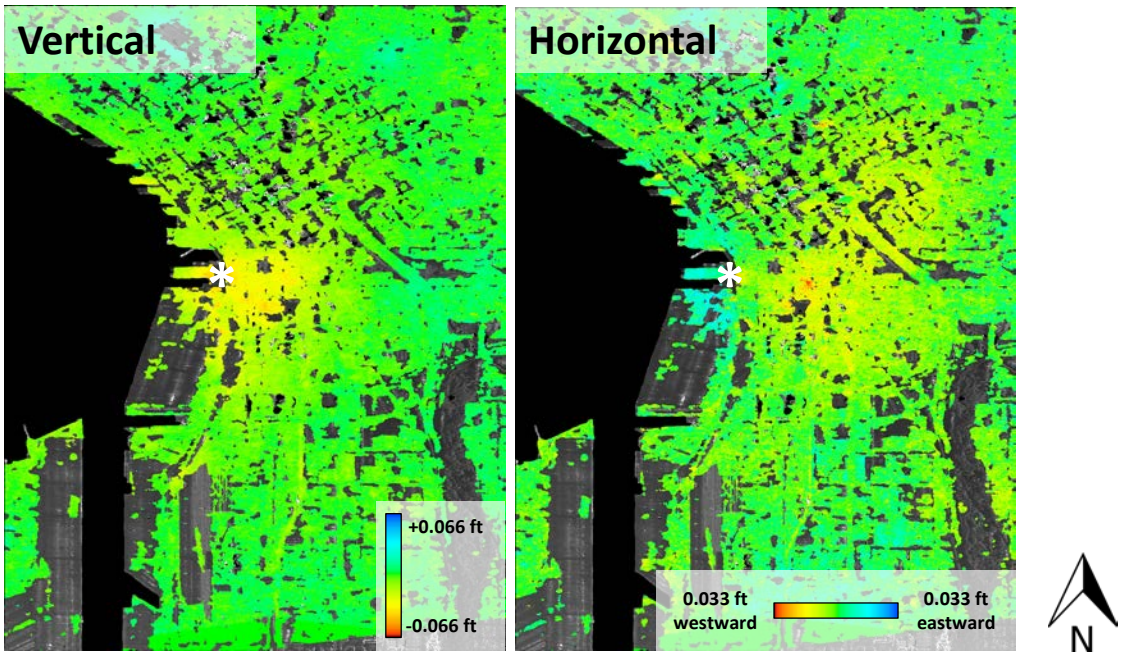

Figure 5-11 Tunnel boring, cutter head failure and initial dewatering cumulative deformation maps (27/07/2014 – 26/10/2014). Location of rescue shaft is denoted with an asterisk.

Figure 5-12 shows the cumulative deformation corresponding to the major dewatering event that occurred to allow for digging a rescue shaft and repair of the boring machine. The cumulative motion in the vertical direction is ~0.11 [ft] and ~0.05 [ft] for the east-west component. The east-west motion pattern is not directly aligned in the east-west direction but show an inclination that may suggests some anisotropy in the affected aquifer.

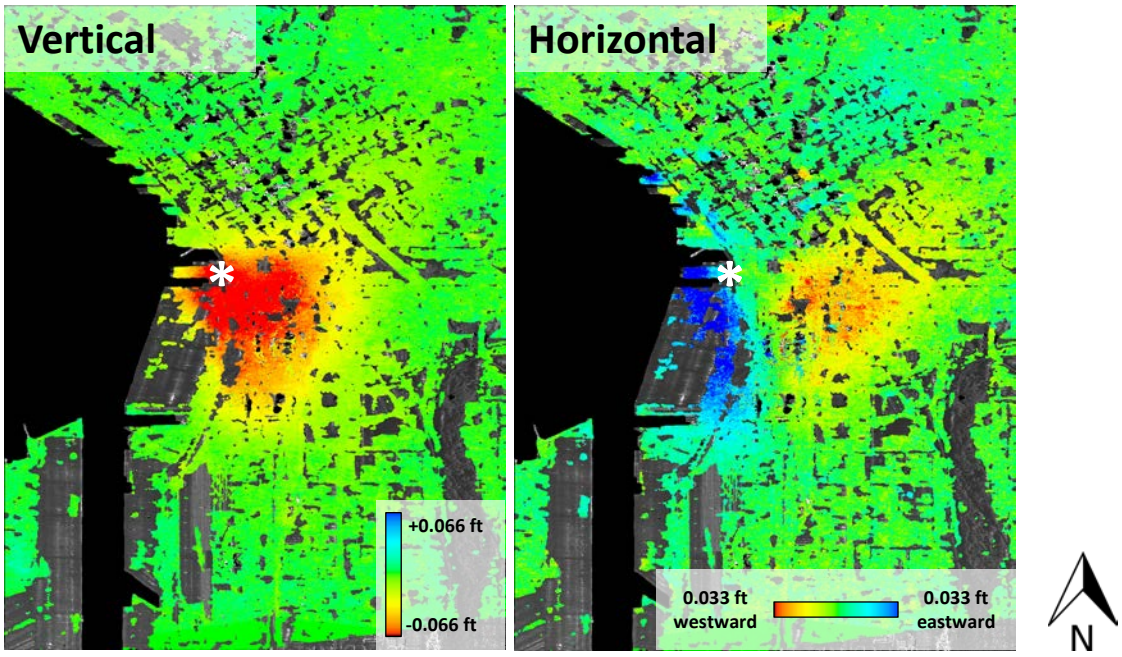

Figure 5-12 Cumulative deformation maps spanning the major dewatering up to tunnel boring restart (26/10/2014 – 01/01/2016). Location of rescue shaft is denoted with an asterisk.

Finally the cumulative deformation in Figure 5-13 from the restart of tunnel boring to the end of the processed RADARSAT-2 data shows a rebound occurring due to the cessation of dewatering. The vertical component shows ~0.1 [ft] of cumulative uplift and the east-west component shows horizontal contraction. From the overall cumulative deformation from 06/06/2014 to 27/07/2016 (Figure 5-9) and the magnitude of the cumulative deformation from 01/01/2016 to 11/07/2016 it is clear that the deformation rebounds to near pre-dewatering levels.

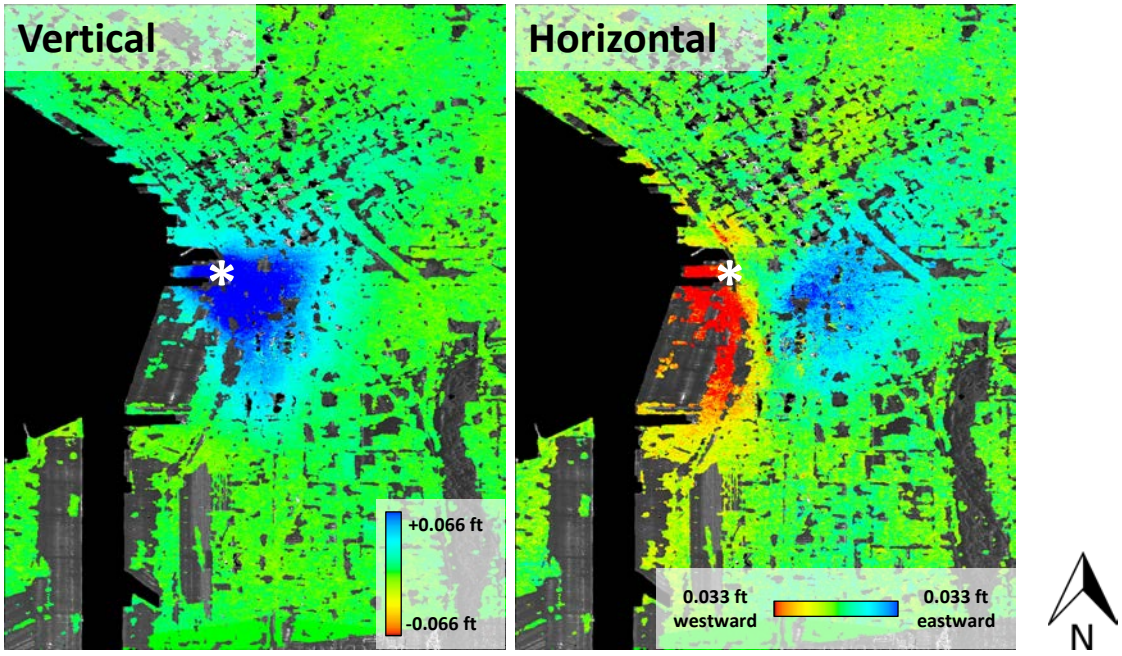

Figure 5-13 Cumulative deformation from the restart of tunnel boring to the end of the processed data (01/01/2016 – 11/07/2016). Location of rescue shaft is denoted with an asterisk.

5.1.6 Deformation Time Series

The 2D multi-temporal deformation estimates correspond to a vertical and an east-west deformation time series for every spatial target in the scene. Figure 5-14 shows some examples superimposed on the vertical linear component coefficient map for each point. Note that these time histories are shown with the thermal model component removed. The rendered points correspond to unfiltered deformation estimates while the continuous curves correspond to temporally low-pass filtered estimates. This low-pass filter is applied to suppress contributions from residual atmospheric phase which is expected to be temporally uncorrelated.

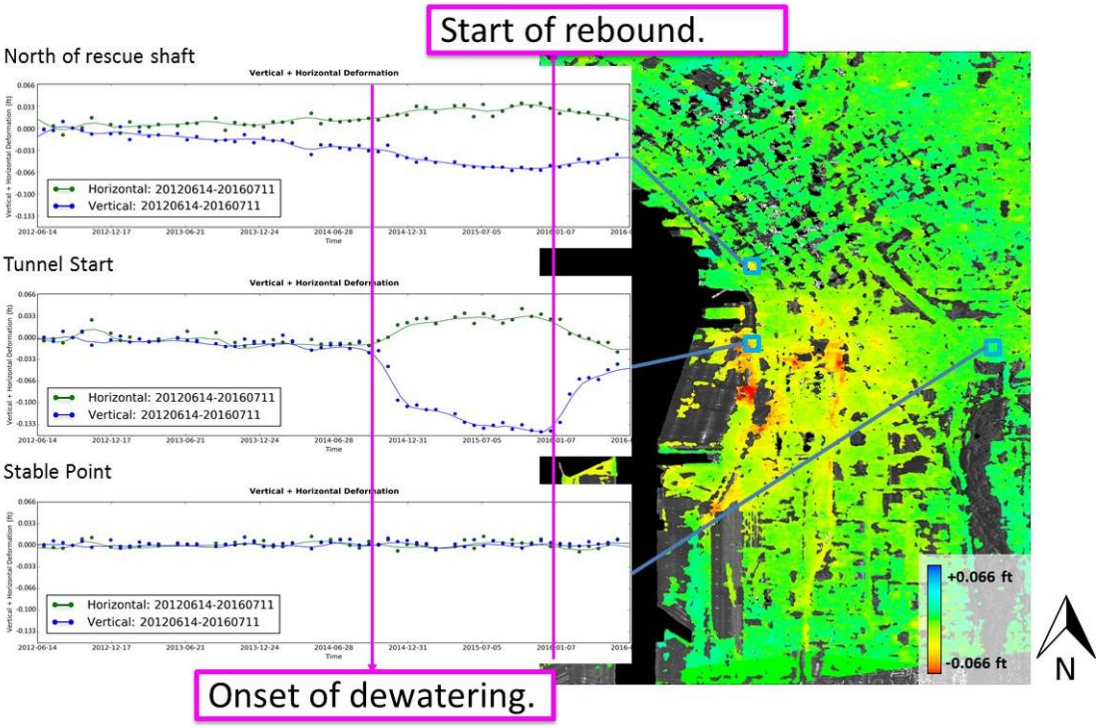

Figure 5-14 2D deformation time series for select points. Plots show unfiltered (points) superimposed with temporally filtered continuous time series.

5.2 Lewistown Narrows, Pennsylvania

This section presents results for InSAR based deformation monitoring of the Pennsylvania Department of Transportation (PennDOT) Route 22/422. Route 22/422 is located between Shade Mountain and the Juniata River in central Pennsylvania. Widening of the highway between Lewistown and Arch Rock interchanges began in spring 2005 and was completed in September 2008 to improve traffic flow and safety. The project included the development of one of the longest mechanically stabilized earth (MSE) walls in the United States.

There is the potential for slope movement along the MSE segments to impact the safety and maintenance of the roadway and therefore these segments are the primary monitoring goal for this project. There are also sections of talus slope that are of secondary monitoring interest.

5.2.1 SAR Data and Processing

One RADARSAT-2 Spotlight stack was acquired in order to monitor the area with potential downslope movement. A summary of the characteristics of the stack is given in Table 5-2. Spotlight data have a resolution of 5.2 [ft] in slant range and 2.6 [ft] in

azimuth (i.e. along satellite track) directions. These data were multi-looked during processing to produce images that have ~10 [ft] resolution in both ground range and azimuth directions. Figure 5-15 shows the ground footprint of SLA75 stack and the processed area of interest, which includes Route 22/422, Shade and Blue Mountain slopes, the railway and Lewistown.

We processed 17 Spotlight RADARSAT-2 ascending scenes spanning the 2015-2016 time intervals. A connected network of 124 interferograms was used. The topographic phase contribution was removed using a 4 [ft] resolution 2006-2008 LiDAR DEM obtained from the PAMAP-Digital Base Maps for Pennsylvania from the Pennsylvania Department of Conservation and Natural Resources [R-3]. The data is also available at the Pennsylvania Spatial Data Access from Pennsylvania State University. National Oceanic and Atmospheric Administration (NOAA) historical temperature [R-4] measurements at Sunbury (40 miles NE from Lewistown) were used to estimate the thermal dilation coefficient.

Table 5-2 Characteristics of Lewistown Narrows RADARSAT-2 Stack

	Beam Mode
	SLA75
Look Direction	Asc
Centre incidence angle [º]	25.7
Ground-range resolution [ft]	9.8
Azimuth resolution [ft]	2.6
Rng x Az swath [miles]	14x5
Number of scenes	18
Stack Start date	Jun-2015
Stack End date	Aug-2016

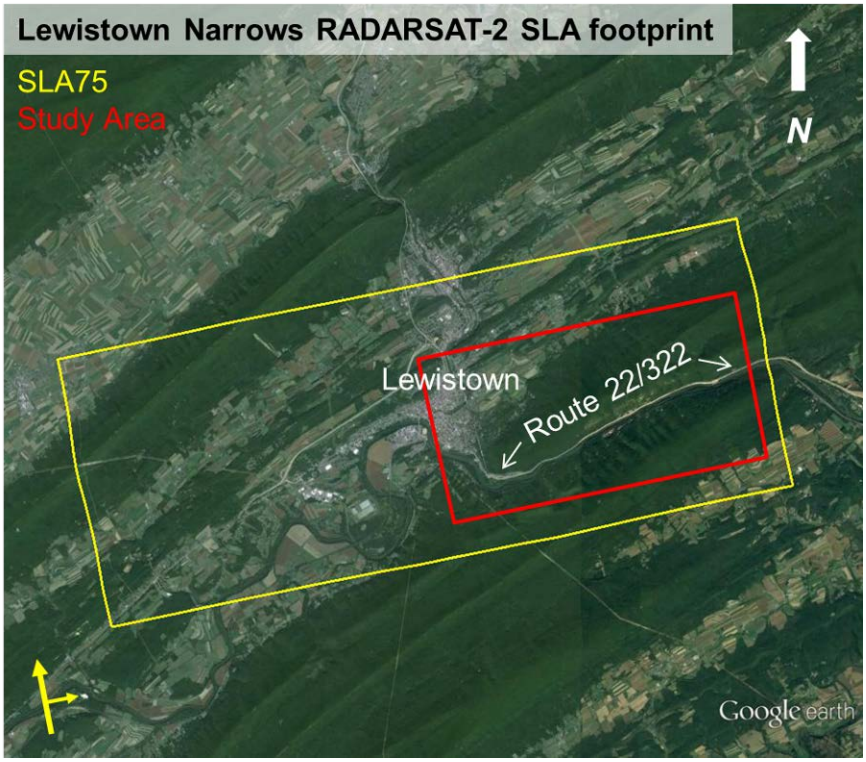

Figure 5-15 RADARSAT-2 acquisition footprint over Lewistown Narrows overlaid on Google Earth optical imagery.

5.2.2 Line-of-Sight Deformation

The ascending stack was processed with the HDS-InSAR to generate multi-temporal line-of-sight (LOS) deformation estimates. Figure 5-16 shows the spatial extent of the linear rate map for the 2015 to 2016 acquisition period. Note that positive values correspond to velocity estimates toward the sensor and negative values correspond to velocity estimates away from the sensor.

Our main goal was to identify slope movement along the MSE segments over Route 22/422, or identify slope instability in Shade or Blue Mountain slopes. One concern over this site at the beginning of the project was the availability of coherent targets in the areas of interest due to the presence of dense vegetation and snow coverage during winter scenes. Our results shows that coherence over Route 22/422 and the railway is high and a large number of targets pass the point selection step, therefore the technique is capable of monitoring the highway over the entire year without significant interruptions.

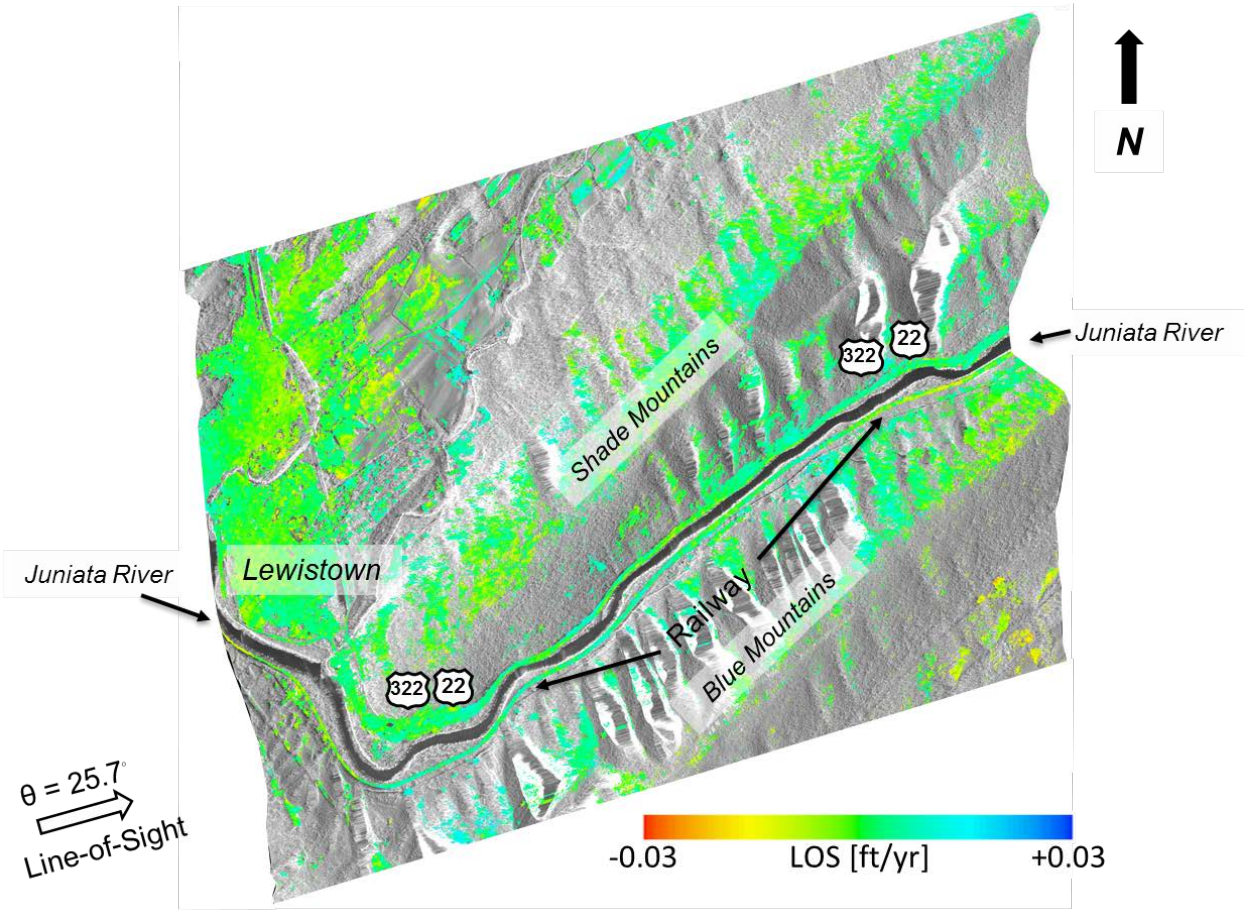

Figure 5-16 LOS linear rate for stack SLA75 (Jun/2015 – Aug/2016).

The LOS linear rate map does not reveal any evidence of significant localized displacement over Route 22/422. Subtle variations of velocity are observed at intermediate wavelength scales. Figure 5-17 shows a LOS sensitivity map to corroborate if the selected stack would be sensitive to downslope movement. This plot also shows the approximate locations of the retaining wall along Route 22/422. Results show that stack SLA75 should be sensitive (>0.7) to deformation occurring over the SE dipping Shade Mountain slope. Sensitivity over the retaining wall is low (~0.4) compared to the sensitivity over Shade Mountain slope. This viewing geometry would be sensitive to subsidence but less sensitive to SE tilting of the wall.

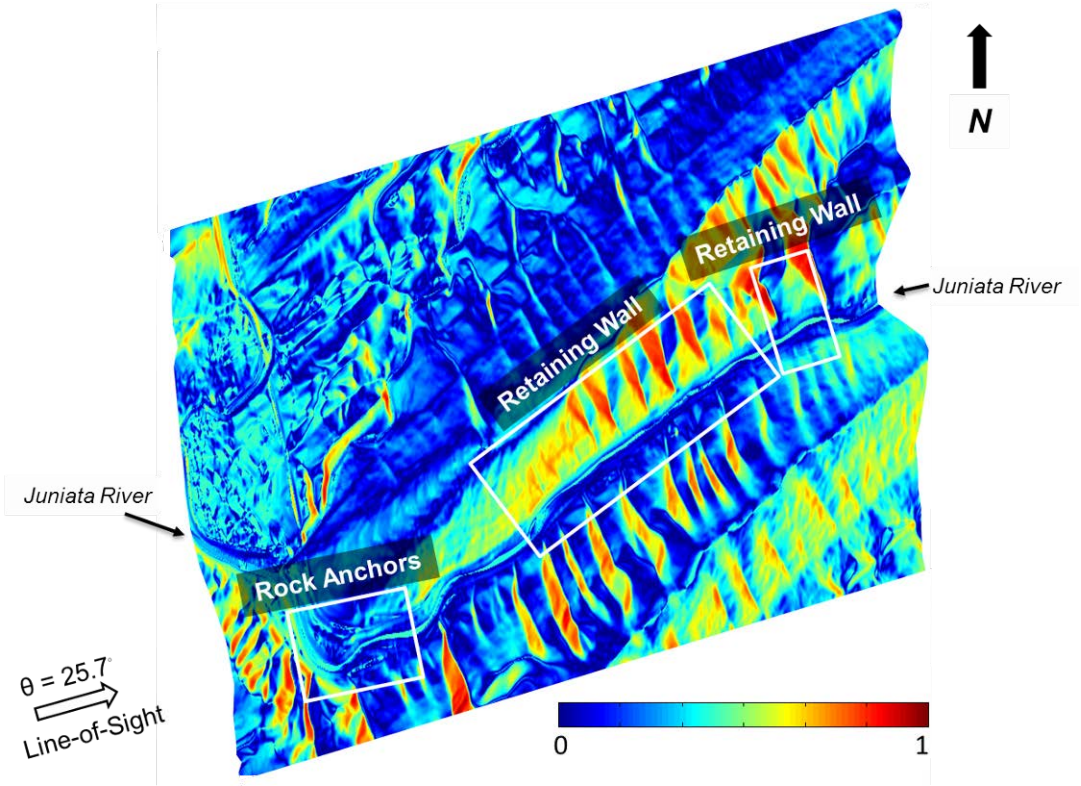

Figure 5-17 LOS sensitivity map for stack SLA75. White boxes indicate the location of the retaining wall and rock anchors.

Figure 5-18 shows a subset over the LOS linear rate map for better analysis of the results. The first three areas (from west to east) denoted by the red circles show regions where subtle intermediate wavelength deformation occurs (0.01 [ft/yr]) over the highway and railway. The deformation time series histories at locations A and B show correlated signals. It is not likely that similar patterns of deformation occur over completely independent slopes. These areas most likely represent residual atmospheric phase rather than real deformation. On the contrary, the red circle in the east shows a portion (0.4 miles) of the railway where 0.02 [ft] subsidence or line-of-sight increase occurs from summer of 2015 to May 2016.

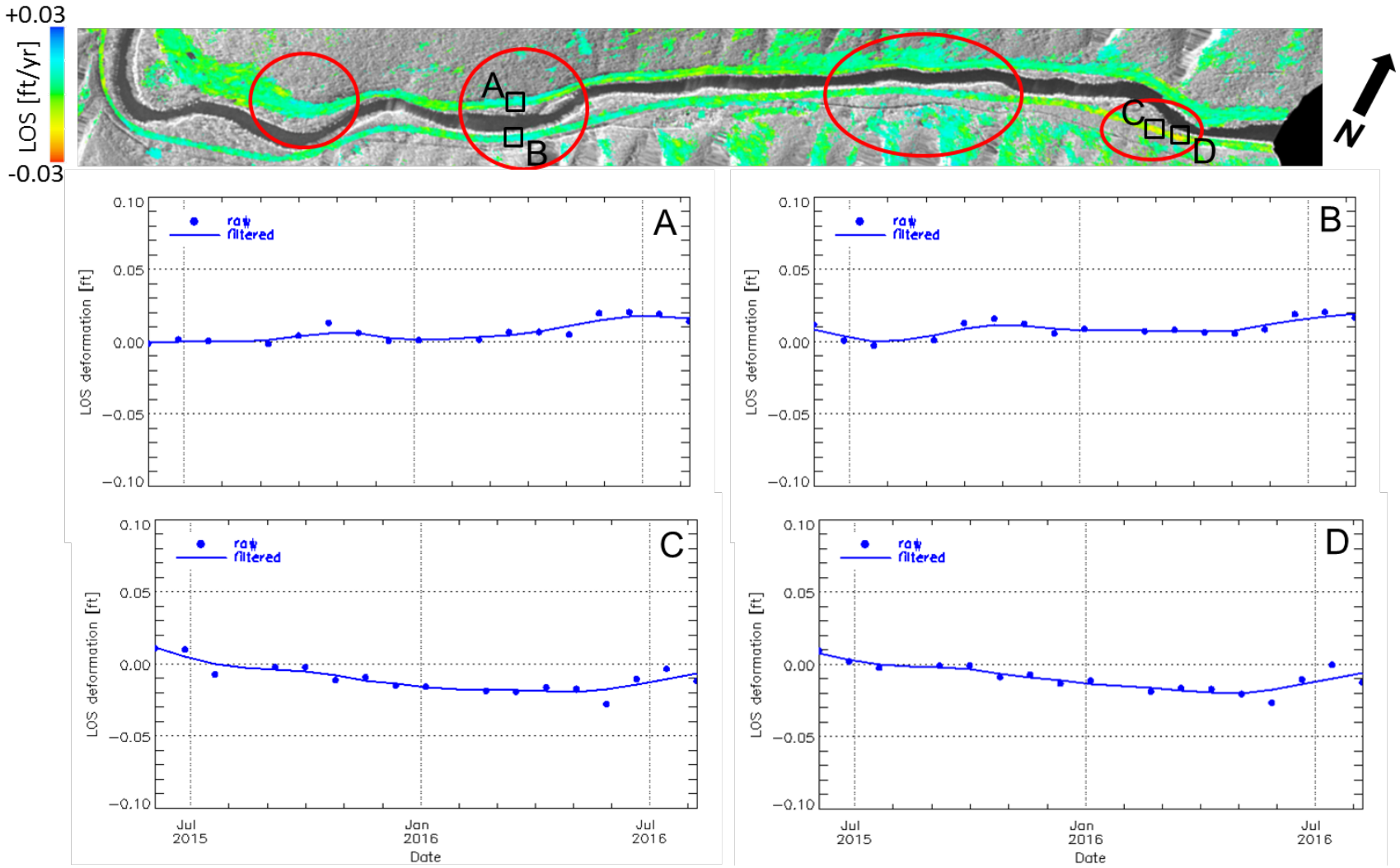

Figure 5-18 Top panel: LOS linear rate map over Route 22/422. Central left and right panels: Deformation time series histories over select points over (A) Route 22/422 and the (B) railway. Bottom left and Deformation time series histories over select points over the railway.

5.3 Bushkill Creek, Pennsylvania

This section presents results for InSAR based deformation monitoring of the Pennsylvania Department of Transportation (PennDOT) Bushkill Creek site. This area lies in a karstic region in the county of Northampton in the state of Pennsylvania. Since 2000 an unusual number of sinkholes have formed [R-5]. The formation of sinkholes produces ground subsidence due to the removal of material or soil in the subsurface and results in primarily vertical displacement. Their formation can cause severe damage to infrastructure as has been verbally reported to the project team by PennDOT.

5.3.1 SAR Data and Processing

One RADARSAT-2 Spotlight stack was acquired in order to monitor the area with potential sinkhole activity. A summary of the characteristics of the stack is given in Table 5-2. Spotlight data have a resolution of 5.2 [ft] in slant range and 2.6 [ft] in azimuth (i.e. along satellite track) directions. These data were multi-looked during processing to produce images that have ~10 ft resolution in both ground range and azimuth directions. Figure 5-19 shows the ground footprint of SLA9 stack. We processed the full scene, which mostly includes the state of Pennsylvania and a small portion of New Jersey.

We processed 17 Spotlight RADARSAT-2 ascending scenes over Bushkill Creek site in eastern Pennsylvania spanning the 2015-2016 time intervals. A connected network of 147 interferograms was processed; however we reduced our network to 47 interferograms to remove unwrapping errors. The topographic phase contribution was removed using a 4 [ft] resolution 2006-2008 LiDAR DEM obtained from the PAMAP-Digital Base Maps for Pennsylvania from the Pennsylvania Department of Conservation and Natural Resources. The data is also available at the Pennsylvania Spatial Data Access from Pennsylvania State University. National Oceanic and Atmospheric Administration (NOAA) historical temperature measurements at Lehighton (18 miles NW from Nazareth) were used to estimate the thermal dilation coefficient.

Table 5-3 Characteristics of Bushkill Creek RADARSAT-2 Stack

	Beam Mode
	SLA9
Look Direction	Des
Centre incidence angle [º]	47
Ground-range resolution [ft]	8.9
Azimuth resolution [ft]	2.6
Rng x Az swath [miles]	14x6
Number of scenes	18
Stack Start date	Jun-2015
Stack End date	Aug-2016

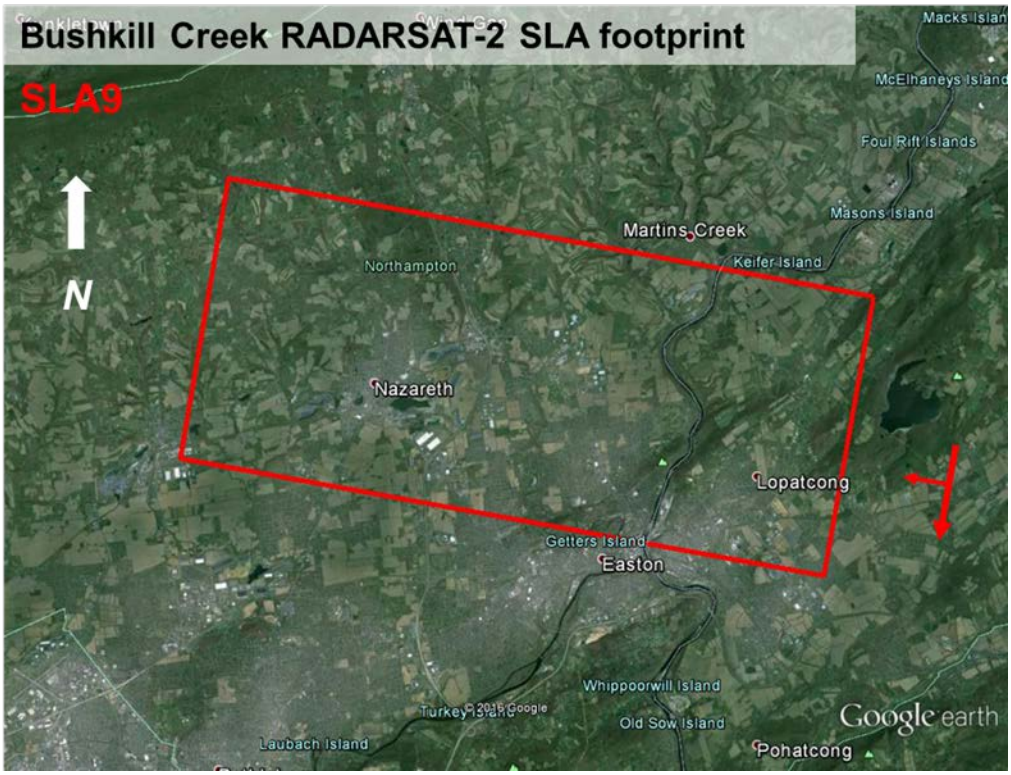

Figure 5-19 RADARSAT-2 acquisition footprint over Bushkill Creek test site overlaid on Google Earth optical imagery.

5.3.2 Line-of-Sight Deformation

The descending stack was processed with the HDS-InSAR to generate multi-temporal line-of-sight (LOS) deformation estimates. Figure 5-20 shows the spatial extent of the linear rate map for the 2015 to 2016 acquisition period. Note that positive values correspond to velocity estimates toward the sensor and negative values correspond to velocity estimates away from the sensor. Black continuous lines show the location of main and secondary roads, as well as rail lines. The road information was obtained from The Pennsylvania Spatial Data Access portal [R-8]. The red dashed line marks the limit between the state of Pennsylvania and New Jersey.

The velocity map shows near zero values at long and intermediate wavelengths, however several areas with short scale deformation signals show linear rates below -0.04 [ft/yr]. We expect that deformation associated with sinkhole activity would be experiencing subsidence or line-of-sight range increase. Since the main goal is to identify any signal associated with sinkhole activity, we apply a threshold to the linear rate map to mask out velocities above -0.01 [ft/yr] and isolate signals that could experience deformation associated with sinkhole activity.

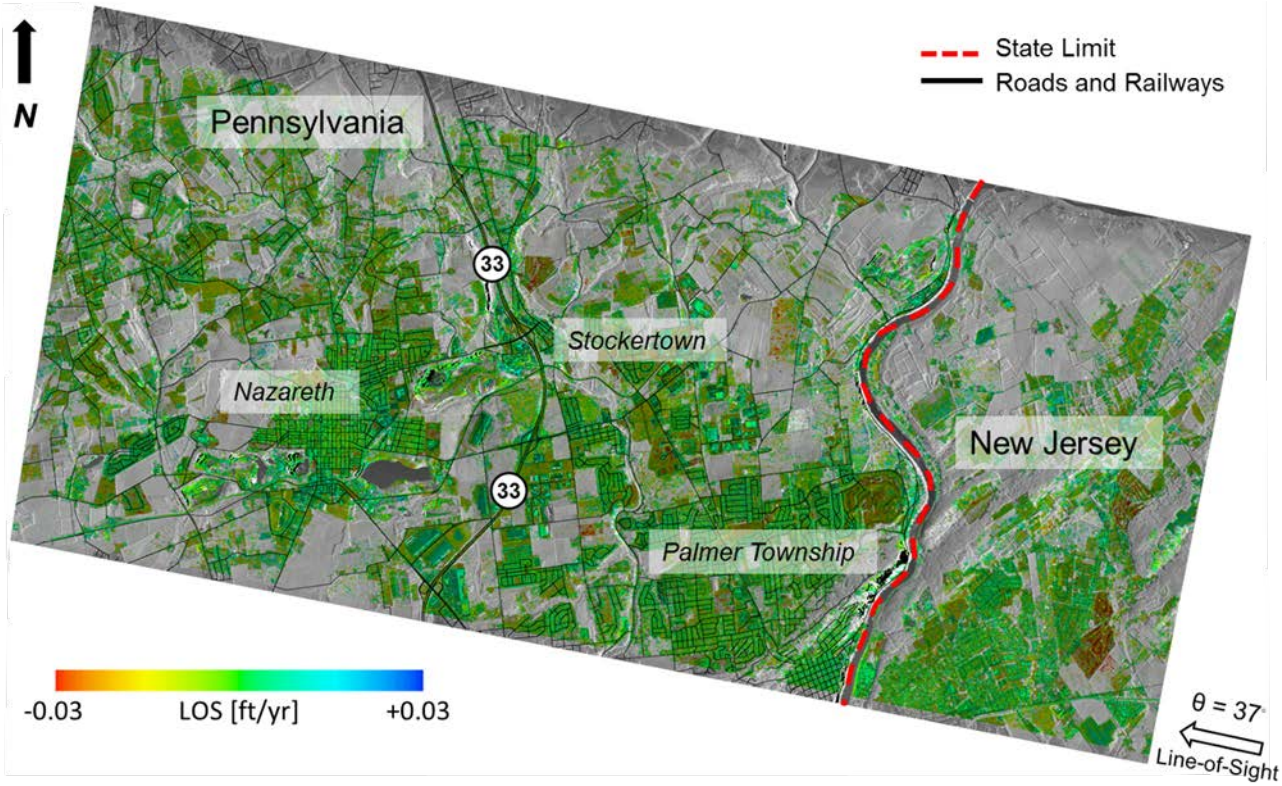

Figure 5-20 LOS linear rate for stack SLA9 (Jun/2015 – Aug/2016).

5.3.3 Deforming Areas

We identified several areas experiencing different types of deformation. In the following section we provide some examples of the observed deforming signals to provide an overview of InSAR capabilities to monitor deformation associated with different physical phenomena. The yellow boxes of Figure 5-21 show the location of some of these regions.

1. Mining Activity

We identify multiple signals experiencing line-of-sight range increase and decrease over the quarry located in Stockertown (~1 mile west of Route 44) (Figure 5-22). These deformation patterns are usually associated with the pumping of groundwater for the extraction of material, therefore causing vertical movements (mostly subsidence). Some areas over the quarry have experienced up to 0.04 [ft] subsidence in one year.

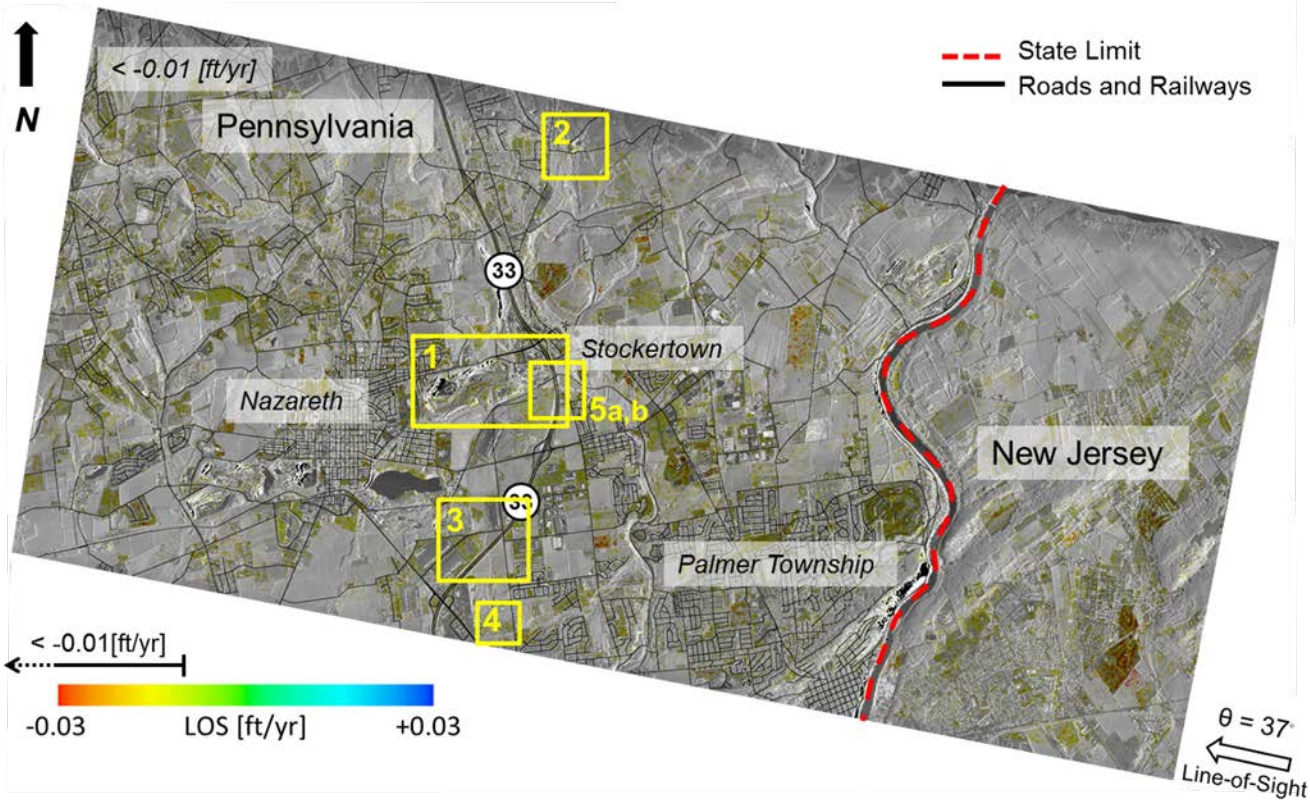

Figure 5-21 LOS linear rate for stack SLA9 after masking out velocities above -0.01 [ft/yr] (Jun/2015 – Aug/2016). Yellow boxes indicate areas analyzed in this document.

1) Slope Instability

We identified a slope experiencing line-of-sight range increase or downslope movement approximately 1 mile east of the town of Belfast, PA (Figure 5-23). The slope is located

east of Weiss Road and north of Engler Road. This area has experienced approximately 0.06 [ft] continuous subsidence in one year.

2) Infrastructure

We identify several spots experiencing subsidence between the northbound and southbound of Route 44 approximately 2 miles southeast from Nazareth (Figure 5-24). Approximately 0.05 [ft] subsidence occurred between summer to fall of 2015 and 0.05 [ft] between the end of winter and summer of 2016. We lack ground truth to corroborate whether these signals represent a precursor that could be associated with sinkhole activity. However PennDOT has indicated that these occur in a sinkhole prone area.

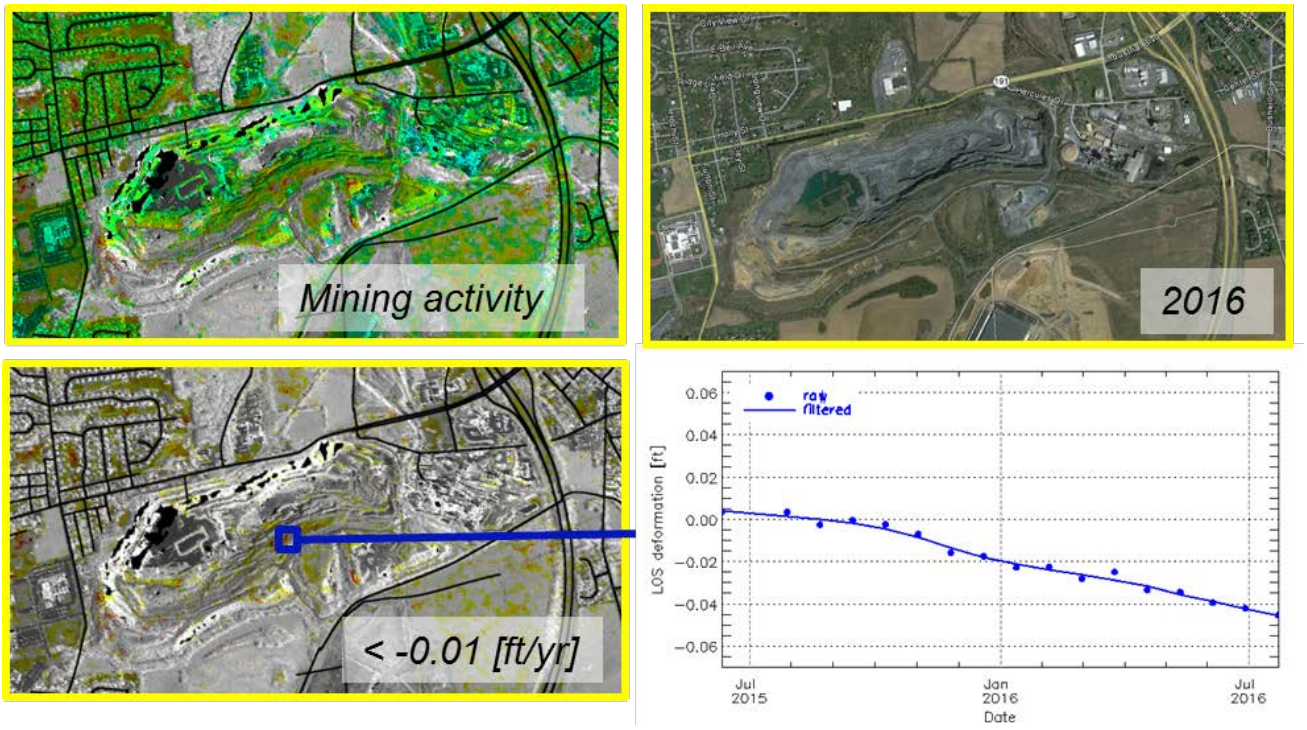

Figure 5-22 Mining activity in Stockertown (Jun/2015 – Aug/2016). Top left panel: LOS linear rate. Bottom left panel: LOS linear rate after masking out velocities below -0.01 [ft/yr]. Top right panel: Google Earth optical imagery. Bottom right panel: Deformation time series histories over a select point over the mine.

3) Infrastructure Settling

East of the intersection of Route 44 and Easton Nazareth Highway we identify subsidence associated with settling of three four story buildings (Figure 5-25). Based on Google Earth optical imagery the buildings were constructed sometime between 2014 and mid-2015. The deformation time series reveals 0.05 [ft] subsidence from July 2015 to February 2016. After February 2016 the area becomes stable.

5a) Sinkhole Activity

South of Stockertown, approximately 0.1 miles southeast from the SR44 Bridge over Bushkill Creek, a subsiding signal was identified just north of Babbling Brook Road (Figure 5-26). The deformation time series shows 0.04 [ft] subsidence from January to August 2016. Based in historical optical imagery from Google Earth a gradual demolition of houses has occurred since 2005 in this area. The presence of ground depressions is evident in the optical scenes.

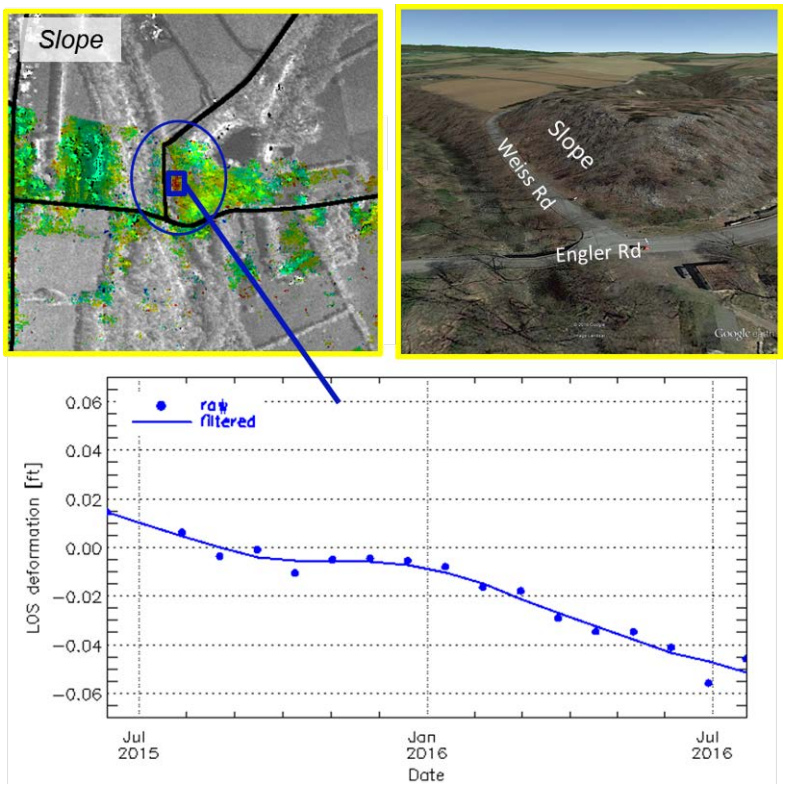

Figure 5-23 Slope instability east of Belfast, PA (Jun/2015 – Aug/2016). Top left panel: LOS linear rate. Top right panel: Google Earth optical imagery. Bottom panel: Deformation time series histories over a select point over the slope.

5b) Infrastructure

We identified a subsiding signal over the northbound and southbound lanes of the SR44 Bridge over Bushkill Creek from July 2015 to August 2016 (Figure 5-27). For verification and comparison to current monitoring activities, we compared InSAR displacement results with survey data provided from PennDOT. Eight survey points are available for comparison. The survey points are distributed in the following order: 4 survey points in the northbound, with two points north of the bridge and two points south of the bridge; and same configuration for the southbound.

The survey points include east, north and vertical measurements from June/November 2004 to August 2016. Since InSAR is mostly sensitive to vertical movement, we only used vertical measurement from the survey points to compare with the InSAR deformation time series. To be consistent with InSAR, we projected each survey point

to the radar line-of-sight and only used the survey data measurements starting from May 2015 to August 2016, having a total of 14 measurements for every survey point (~every month).

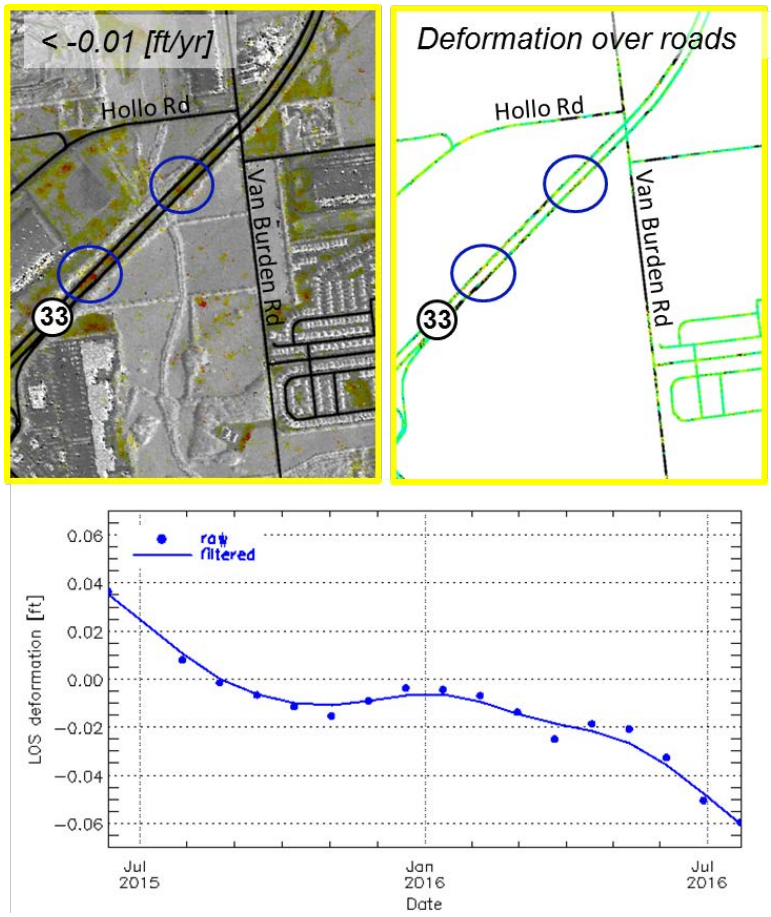

Figure 5-24 Deformation along Route 44 (Jun/2015 – Aug/2016). Top left panel: LOS linear rate after masking out velocities above -0.01 [ft]. Top right panel: LOS linear rate over main and secondary road. Bottom panel: Deformation time series histories over a select point over area experiencing subsidence.

Figure 5-27 shows the location and comparison of the survey points with InSAR. We selected one deformation InSAR time series and compared with the two adjacent survey points north and south of the bridge in the northbound and southbound lanes.

In general a good agreement between the survey points and the InSAR deformation time series exist. A 0.02 [ft] vertical movement (subsidence) exist between summer 2015 to summer 2016. The agreement of InSAR measurements with the survey points is better with the points located north of the bridge. These survey points show small variability between measurements. The agreement of InSAR with the survey points located south of the bridge are also in agreement, but to a lesser degree, however the survey point at these locations show high variability between measurements.

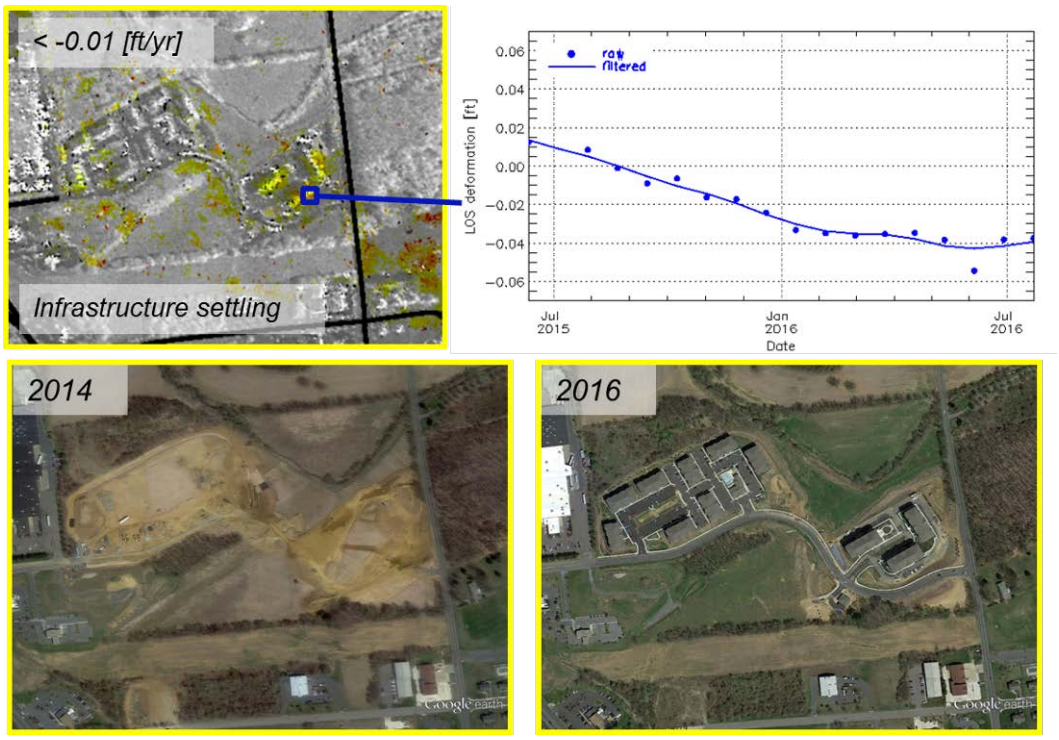

Figure 5-25 Infrastructure settling. Top left panel: LOS linear rate after masking out velocities above -0.01 [ft]. Top right panel: Deformation time series histories over a select point over a building. Bottom left panel: Google Earth optical imagery from 2014. Bottom right panel: Google Earth optical imagery from 2016.

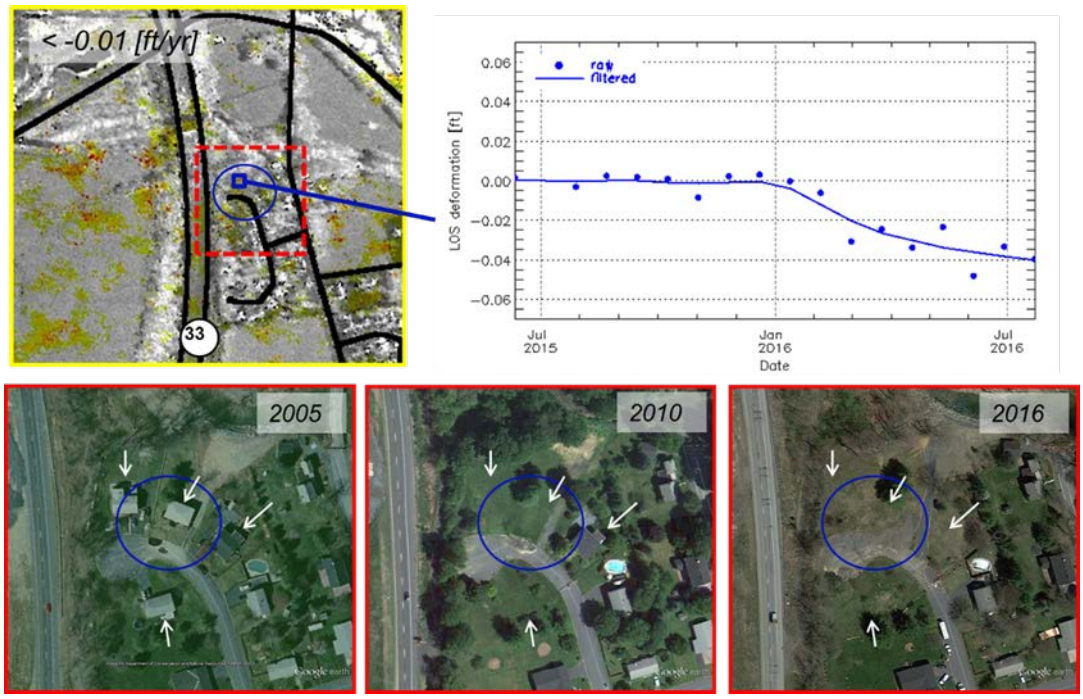

Figure 5-26 Sinkhole activity. Top left panel: LOS linear rate after masking out velocities above -0.01 [ft]. Top right panel: Deformation time series histories over a select point over a region showing depression of ground. Bottom panels: Historical Google Earth optical imagery 2005 (left), 2010 (center) and 2016 (right).

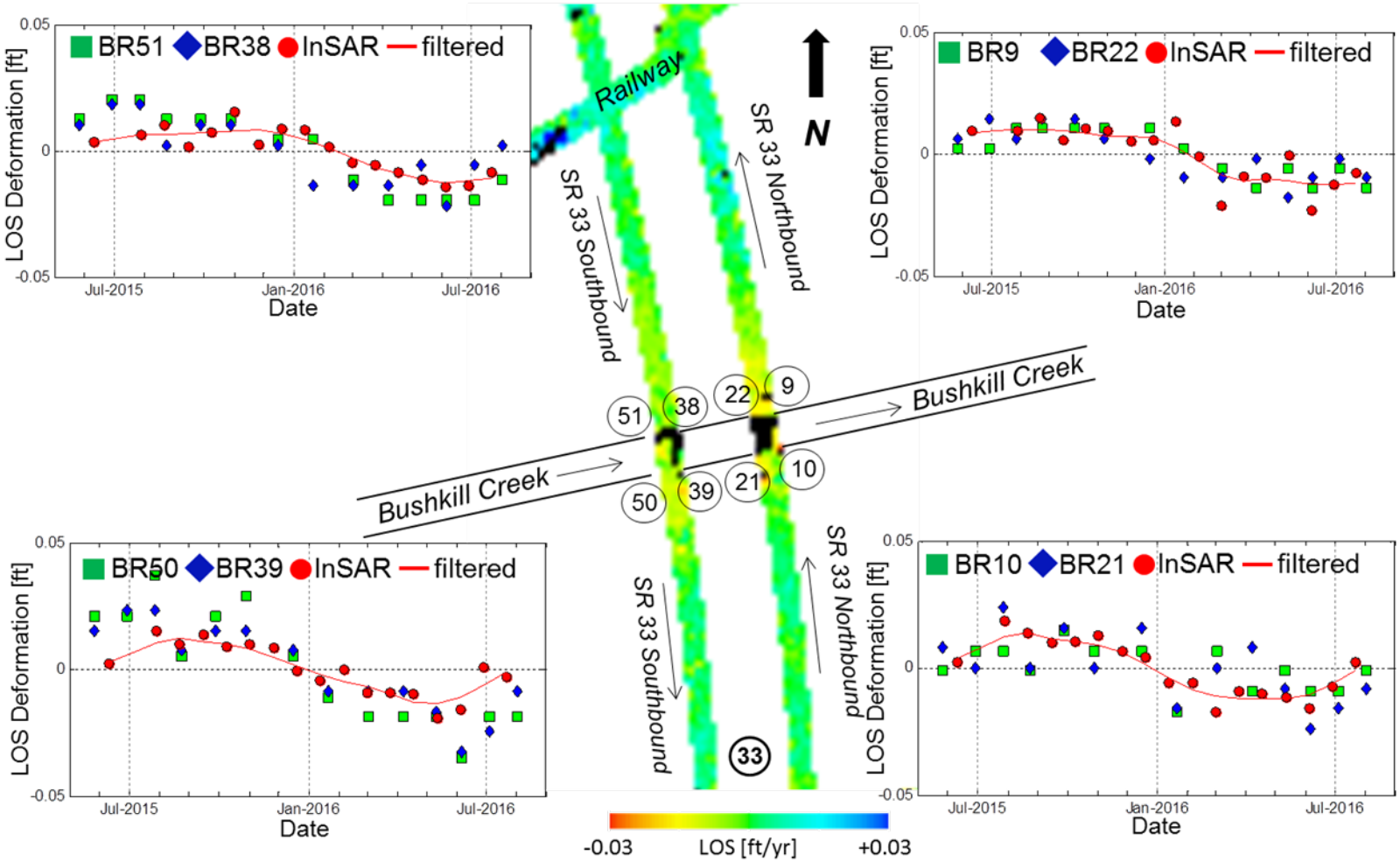

Figure 5-27 InSAR and survey points comparison at SR44 Bridge over Bushkill Creek. Green squares show external survey points and blue diamonds show internal survey points. Red dots show InSAR time series histories and continuous line the InSAR temporal filtered time series histories. The LOS linear rate map over SR44 highway is shown in the center.

5.4 Geysers, California

This section presents results for InSAR based deformation monitoring of the Geysers geothermal field zone. Geysers geothermal field is located in the Macayamas Mountains in California and is the largest single geothermal field in the world [R-6, R-7]. It has been operating for 50 years and currently contains 22 geothermal power plants. It supplies Sonoma, Lake, Mendocino, Marin and Napa counties, accounting 20% of green power generated in the state of California.

The heat source is located ~4.7 miles below the surface and spreads over 45 sq. miles. Steam is transported through pipes and used to spin turbines to generate electricity. The geothermal reservoir is recharged by injecting recycled wastewater from the city of Santa Rosa and the Lake County sewage treatment plants. Deformation patterns in geothermal fields are characterized by multiple up/down cycles which are mainly controlled by the different rates of steam productions and water injection.

5.4.1 SAR Data and Processing

Two RADARSAT-2 Ultra-Fine (UF) stacks were acquired over Cobb to monitor deformation patterns associated with geothermal activity. A summary of the characteristics of the stacks are given in Table 5-4. Ultra-Fine data have a resolution of 5.9 [ft] and 6.2 [ft] in slant range for the ascending and descending scenes respectively, and 9.2 [ft] in azimuth (i.e. along satellite track) direction. These data were multi-looked during processing to produce images that have ~12 [ft] resolution in both ground range and azimuth directions. Figure 5-28 shows the ground footprints of U21 and U25 stacks.

We processed 40 ascending and 42 descending Ultra-Fine RADARSAT-2 scenes over Cobb California spanning the 2014-2016 time intervals. A connected network of 216 interferograms was used for the ascending stack and 429 interferograms for the descending stack. The topographic phase contribution was removed using the 44 [ft] resolution National Elevation Dataset (NED) from the United States Geological Survey (USGS).

Table 5-4 Characteristics of Cobb/Geysers RADARSAT-2 stacks

	Beam Mode	
	U25	**U21**
Look Direction	Asc	Des
Centre incidence angle [º]	47.8	45.4
Ground-range resolution [ft]	5.9	6.2
Azimuth resolution [ft]	9.2	9.2
Rng x Az swath [miles]	14x14	14x14
Number of scenes	40	42
Stack Start date	Jan-2014	Jan-2014
Stack End date	Apr-2016	Apr-2016

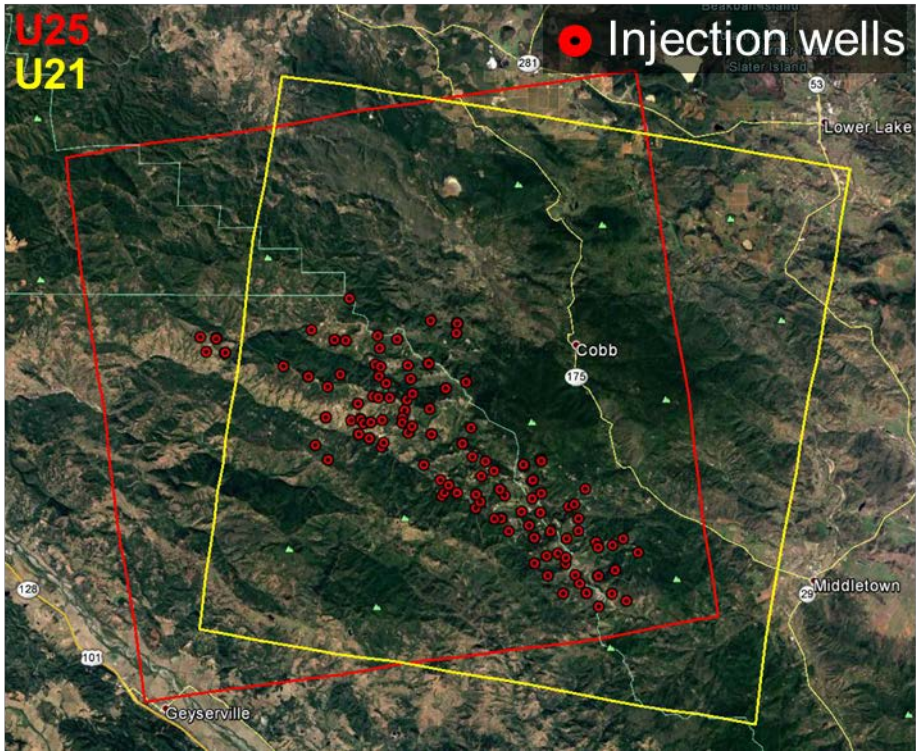

Figure 5-28 RADARSAT-2 acquisition footprint over Geysers Geothermal field overlaid on Google Earth optical imagery. Red dots show the location of the injection wells.

5.4.2 Line-of-Sight Deformation

The ascending and descending RADARSAT-2 Ultra-Fine stacks were processed with the HDS-InSAR to generate multi-temporal line-of-sight (LOS) deformation estimates. Figure 5-29 shows spatial maps of cumulative deformation for the 4 year acquisition

period. The positive values correspond to deformation toward the sensor and negative values correspond to deformation away from the sensor. The deforming areas are in agreement with the locations of the geothermal power plants and injection wells. The deformation patterns between the ascending and descending stacks are roughly in agreement. Some areas show discrepancies which may be associated with horizontal movements, different areas illuminated by the radar and differences derived from the SVD inversion in the evenly sampled U21 stack against the unevenly sample U25 stack.

The descending stack (U21) is roughly evenly sampled in time (every 24 days), however the ascending stack lacks of SAR imagery between mid-2014 to January of 2015 (only 4 scenes from July 2014 to January 2015). Figure 5-30 and Figure 5-31 show the maps of cumulative deformation for different periods of time, in which the temporal distribution of SAR scenes is similar for both stacks. It can be observed that the maps of cumulative deformation are similar for the two periods of time, showing uplift or movement toward the sensor from January 2014 to August 2014, and subsidence or movement away from the sensor from November 2014 to April 2016. These results mainly reflect vertical deformation over the geothermal field, which might be associated with the different rates of steam production and water injection, although ground truth data would be required to confirm this assumption.

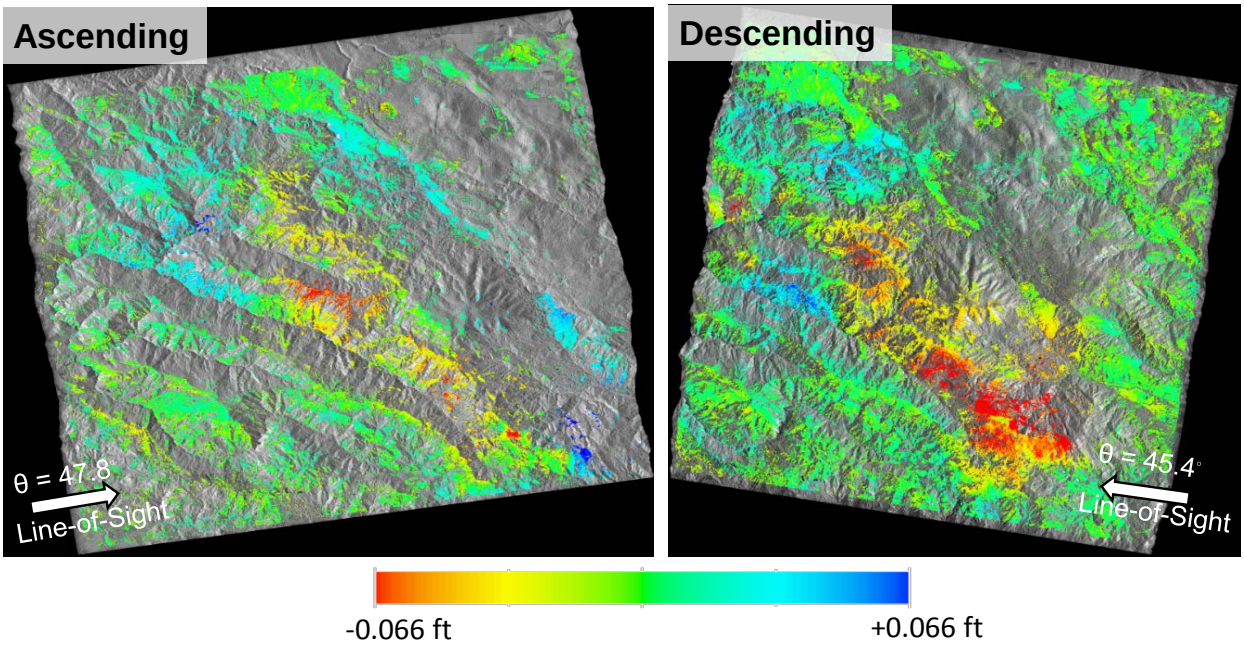

Figure 5-29 LOS cumulative deformation for the two data stacks (Jan/2014 – Apr/2016).

5.4.3 2D Decomposed Deformation

The LOS deformation estimates were decomposed into vertical and east-west estimates for the different periods of time as shown in Figure 5-32. Note that for the vertical case, positive values correspond to uplift and negative values correspond to subsidence.

Deformation over the geothermal field is mostly vertical with cumulative motion of -0.066 to 0.066 [ft]. It is interesting to observe that the horizontal deformation maps also shows residual motion. For the east-west case, positive values correspond to eastward motion and negative values correspond to westward motion. The east-west deformation patterns for the three different periods analyzed are roughly the same even though the directions of the observed vertical movements differ in time. It is very likely that the observed horizontal deformation is associated with geothermal activity since this pattern occurs over the same area of vertical deformation and at the locations of wells and geothermal plants, although ground truth data would be required to confirm this assumption.

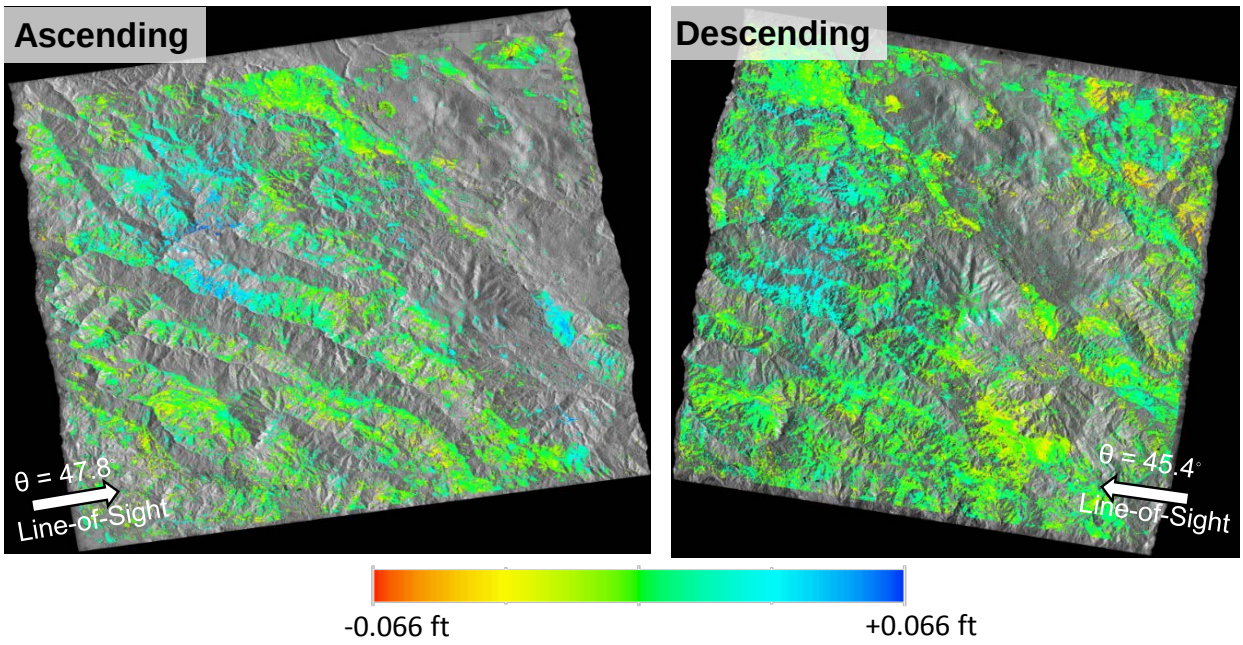

Figure 5-30 LOS cumulative deformation for the two data stacks (Jan/2014 – Aug/2014).

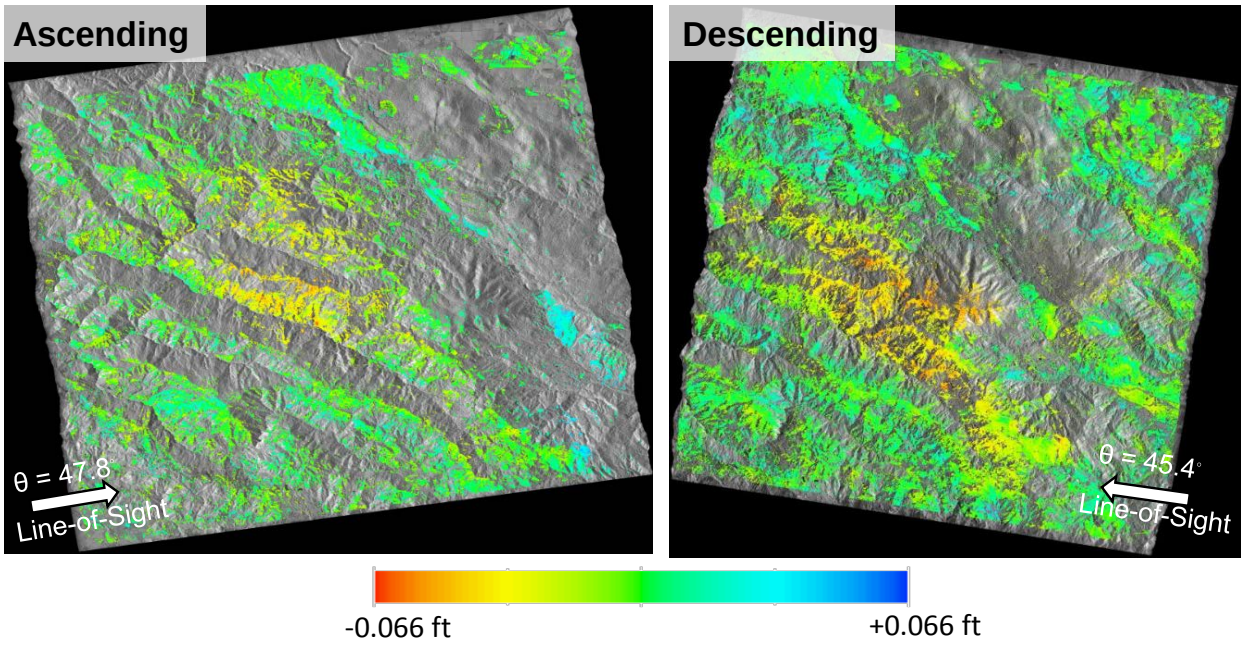

Figure 5-31 LOS cumulative deformation for the two data stacks (Nov/2014 – Apr/2016).

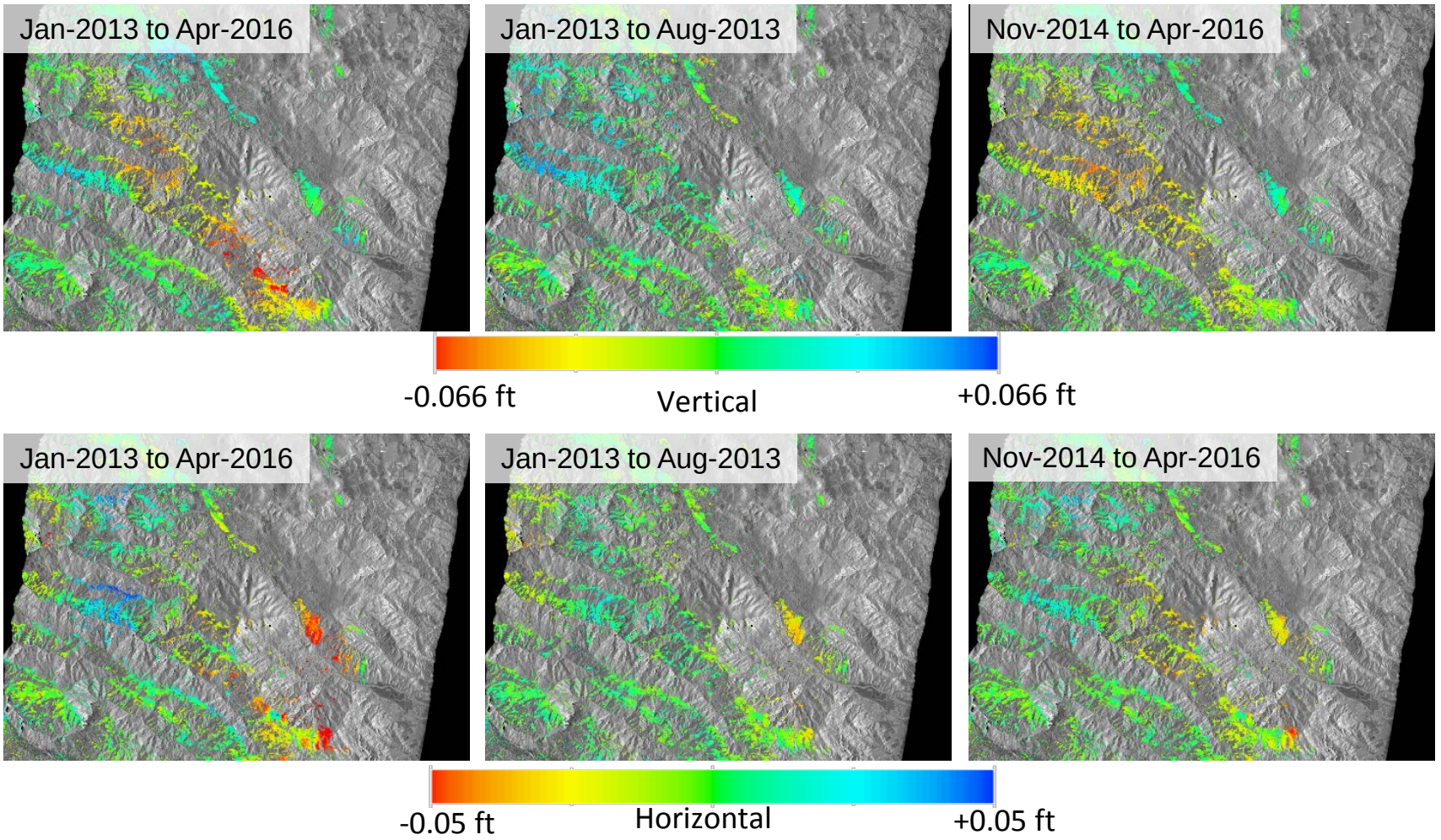

Figure 5-32 2D cumulative deformation. Left panels: deformation for the Jan/2014 to Apr/2016 period. Central panels: deformation for the Jan/2014 to Aug/2014 period. Right panels: deformation for the Nov/2014 to Apr/2016 period.

5.4.4 Deformation over Infrastructure for Transportation

Geysers geothermal field has been active for 50 years and new plants are under construction to meet energy demands. Deformation derived from steam production and water injection will continue while plants are under operation, and damage to infrastructure for transportation could potentially occur. In this section we aim to demonstrate the impact that anthropogenic activity has over man-made structures such highways and roads. Road information was obtained from the GIS databases from Sonoma and Lake Counties [R-9, R-10]. Power plants locations were obtained from [R-11].

Left panel of Figure 5-33 shows cumulative deformation over main and secondary roads for the time period of Jan/2014 to Apr/2016 derived from the descending pass. Portions of the roads marked in black represent areas where InSAR measurements were not available due to low coherence.

The largest highway in this area is State Route 175, which connects the towns of Hopland and Middletown in Mendocino and Lake Counties respectively. This road, which is located approximately 2 miles away from the center of the deforming zone, does not seem to be affected by deformation derived from geothermal activity. However multiple secondary roads, mainly within the geothermal plants zone, are strongly affected by different rates of deformation. It is noteworthy that from the 8,466,620 targets available over the entire scene, 450,158 occur over these roads, demonstrating the potential of HDS-InSAR technique to monitor infrastructure for transportation over large regions. A similar product was also obtained for the ascending stack, in which 196,698 targets over main and secondary roads are available out of the 4,698,447 in total. A more detailed view of the deformation occurring over secondary roads is shown in on the right panel of Figure 5-33.

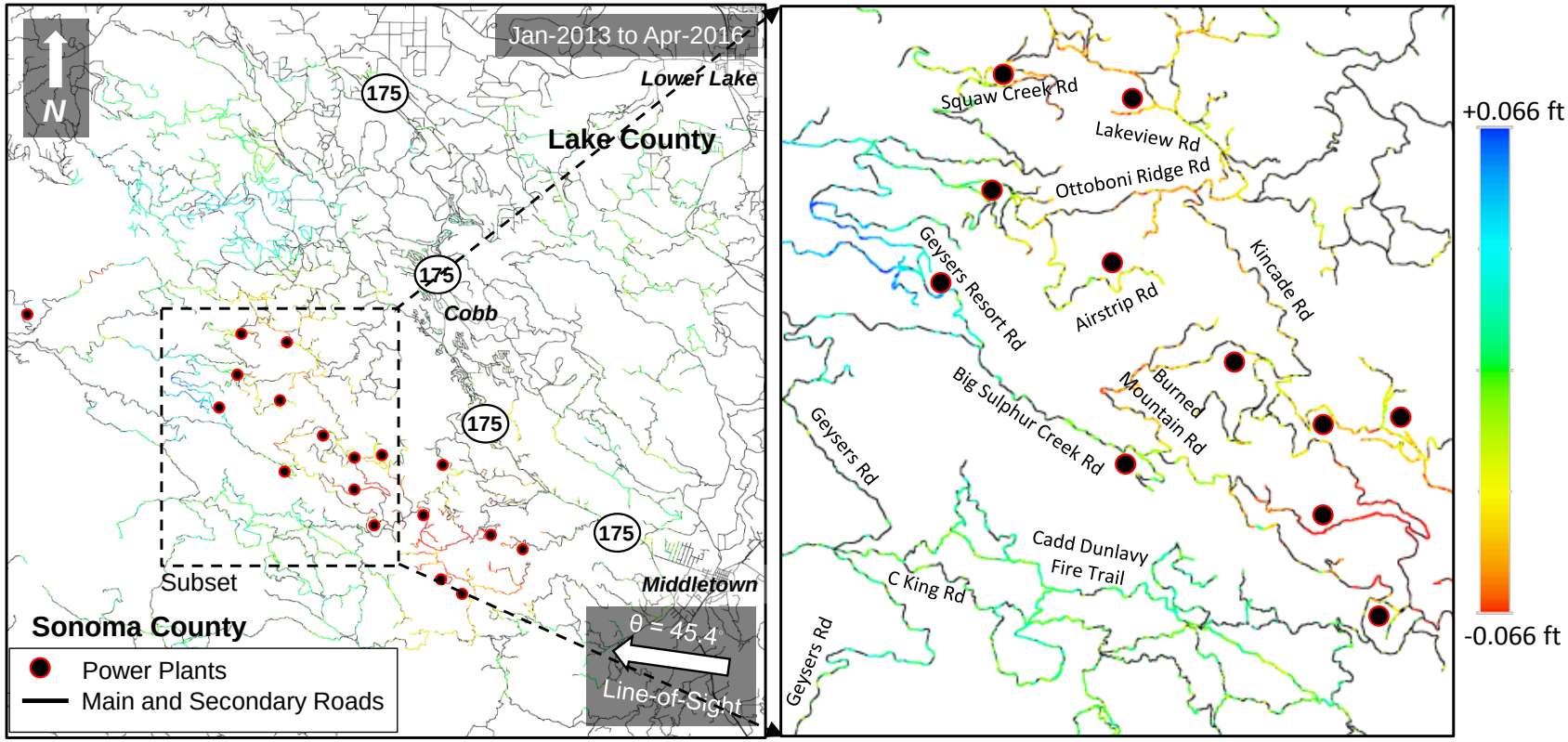

Figure 5-33 Left panel: LOS cumulative deformation for the descending stack (Jan/2014 – Apr/2016) over main and secondary roads. Right panel: LOS cumulative deformation over a subset of the scene. Red dots show the locations of the geothermal plant.

6 INSAR VISUALIZATION TOOL

6.1 Overview

This project included the implementation of an improved Google Earth visualization tool to allow interactive viewing of InSAR deformation results. The focus of the tool is specifically on the visualization of transportation infrastructure so that users can monitor their infrastructure with wide area coverage and view results specific to their interests. The tool that was originally built as an add-on to Google Earth is to allow interactive visualization without the need for GIS specific software. This allows the visualization of InSAR results by non-GIS professionals.

The tool allows for the interactive display of deformation layers and plotting of the time series for a specific spatial data point through Google Earth. The tool prior to transportation specific improvements is shown below in Figure 6-1 where the user can roam around and plot InSAR derived deformation time series for individual spatial points.

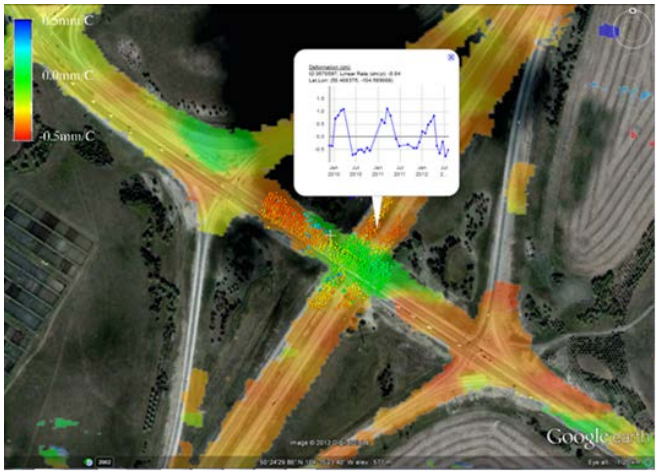

Figure 6-1 Example of baseline Google Earth visualization tool before updates.

The enhancements include allowing for the generation and plotting of data along spatial transects, as specified by the user by either Keyhole Markup Language (KML) files or shape files (SHP) containing the definitions of road (transects). In this way, existing or user defined vector format data defining transportation infrastructure networks can be used to extract either one dimensional transect-following deformation plots or two dimensional maps with non-transport infrastructure areas removed. Figure 6-2 shows an example of a single transect defined in a KML file over Seattle and an example plot showing deformation from the subsidence bowl in February 2015.

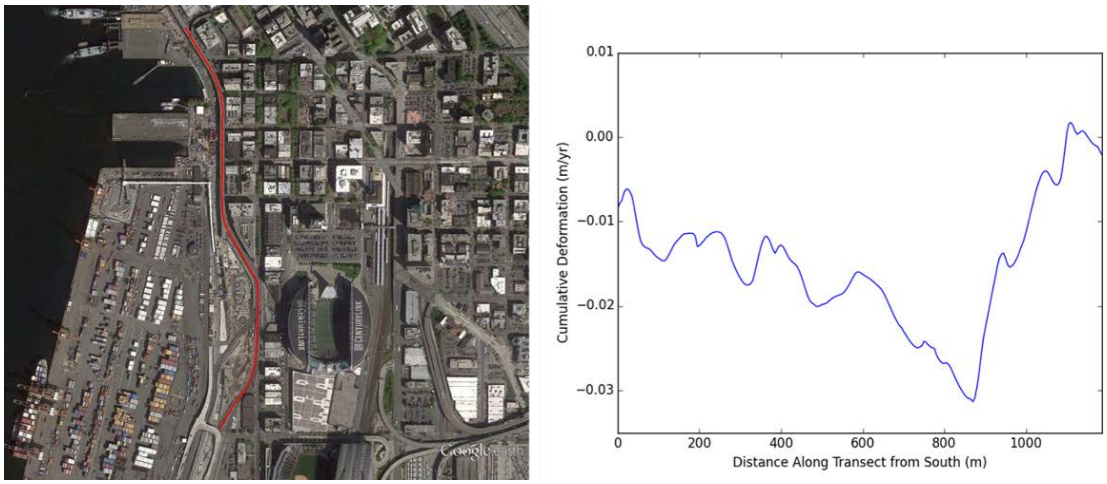

Figure 6-2 Example of user specifying a transect via KML and a 1D plot of example deformation along the transect.

A more complicated network of transects can be defined and used to generate plots and maps over a road network. Figure 6-3 below show an example road network over Seattle extracted from a SHP file and Figure 6-4 shows a 2D deformation map generated from this road network. Finally Figure 6-5 shows an example of arbitrary transects drawn into a KML file and the resulting deformation map.

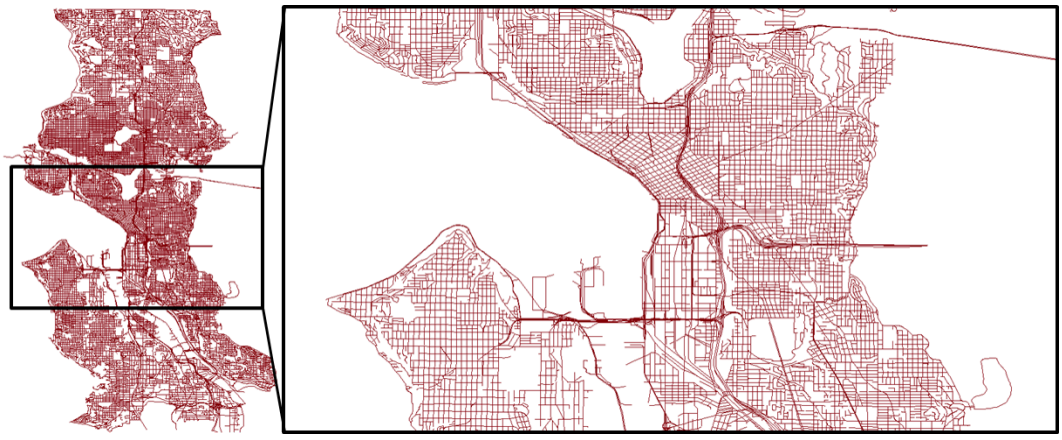

Figure 6-3 Example of a SHP file containing the road network over Seattle.

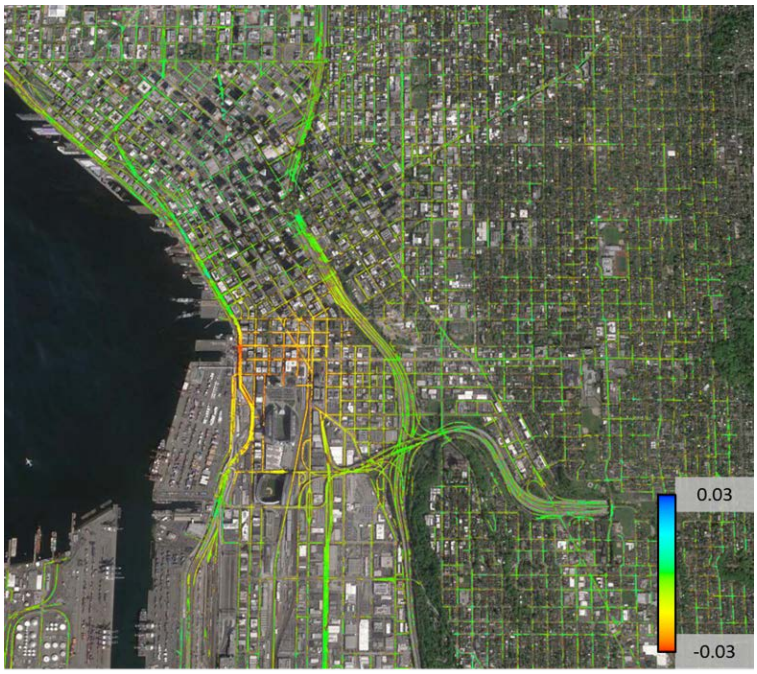

Figure 6-4 Example of extracting a deformation layer along the Seattle road network.

Figure 6-5 Example of defining arbitrary transects in a KML file and extracting the corresponding deformation map.

6.2 Examples

The plug-in includes a graphical user interface (GUI) that allows the user to configure the rendering of data and the plots of time series and transects. An example of the GUI is shown below in Figure 6-6. A default data overlay of the last date layer available in

the time series or as configured by the user is displayed in Google Earth for context, a date showing the subsidence bowl over Seattle is shown in Figure 6-7, and a zoom in showing an interactive plot of a points time series is shown in Figure 6-8.

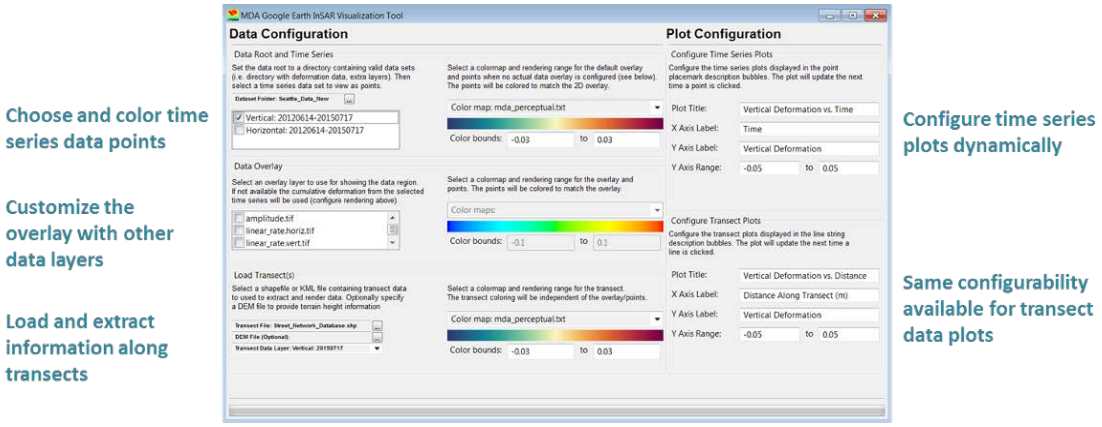

Figure 6-6 Example of the visualization tool UI.

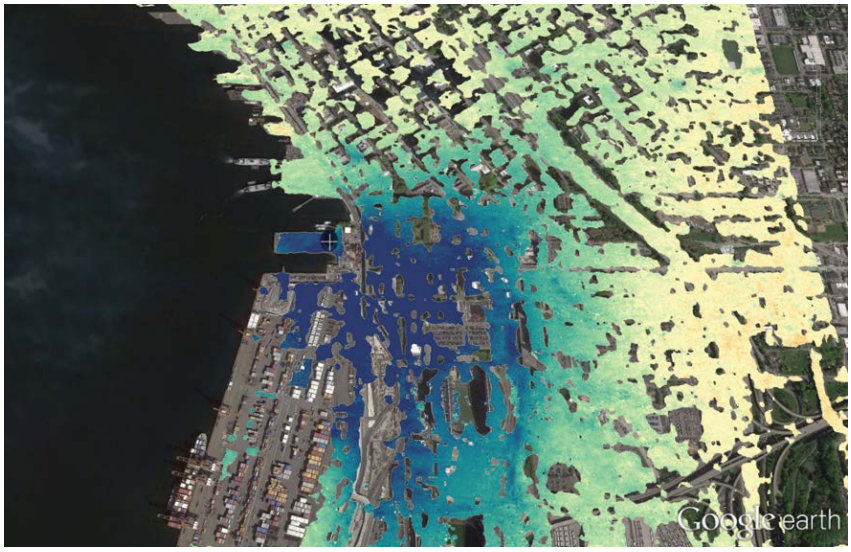

Figure 6-7 Example of a data overlay configured by user and the data cursor plus point within it vicinity (top left of blue region).

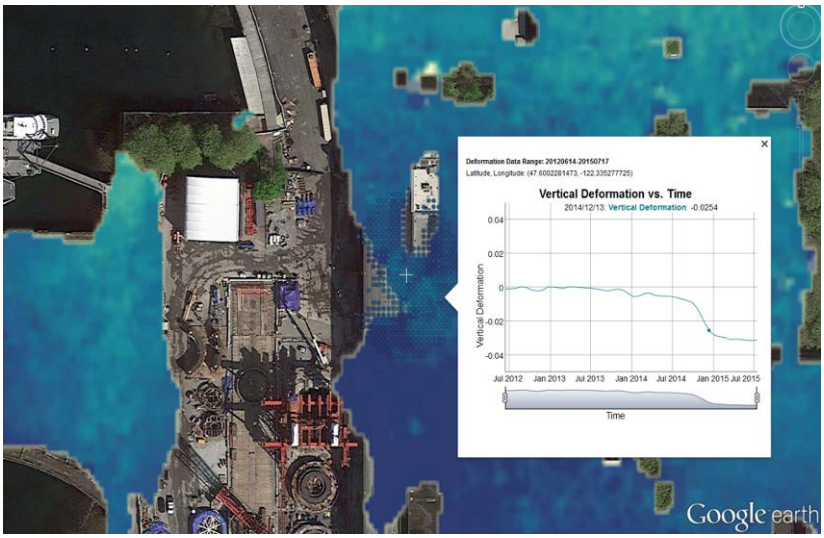

Figure 6-8 A zoom in to where the rescue shaft was dug showing the selectable data point and a time series plot of an example data point.

By configuring a road network a user can interactively click on elements defined in the network and view plots of the deformation along a transect for a given data layer. A two dimensional overlay of the transects for a chosen deformation layer is generated and overlaid with the actual transect vector data which the user can click on to plot information. Figure 6-9 below shows the 2D transect overlay and Figure 6-10 shows an example plot of one of the roads.

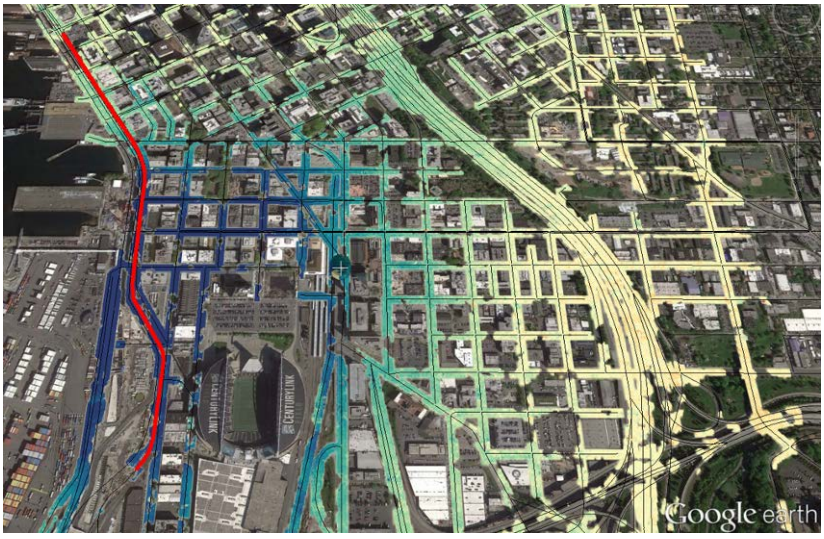

Figure 6-9 Example of extracting the deformation data on the Seattle road network, with overlaid KML lines which are selectable Google Earth features (red line).

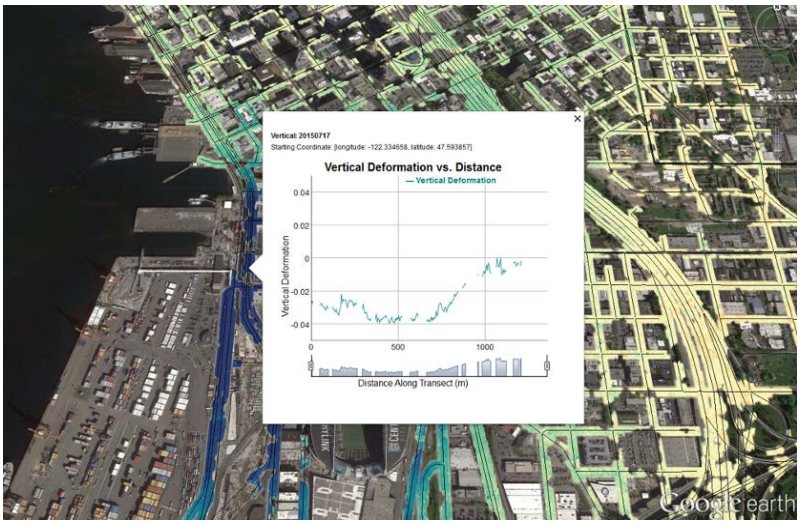

Figure 6-10 Example of clicking on one of the KML lines defining a transect and plotting the deformation data along the transect.

7 CONCLUSIONS

The MDA team combined the existing HDS-InSAR solution along with tools developed during the project to address specific issues associated with urban building topography and monitoring of road networks to achieve a displacement monitoring solution for road and bridge infrastructure. This solution was used to generate deformation results for all four project sites. In combination these results demonstrate the utility of the solution for monitoring of transportations infrastructure for a variety of applications (tunnel construction, slope stability, karstic sinkholes, slope stability, bridges) in an array of terrain, vegetation and climate conditions.

An InSAR visualization plugin for Google Earth was developed with support for monitoring deformation along road segment transects. This tool allows for non-GIS DOT professionals to view, browse and interpret InSAR results with the need for specialize GIS software tools therefore improving accessibility of this technology within state DOTs.

Site specific conclusions are detailed below:

Seattle

Vertical and east-west deformation estimates were generated by processing and combining data from both pass directions. Results include a very high spatial density of targets within the area of interest and show the significant subsidence and subsequent rebound uplift which occurred as a result of site dewatering activities. The results also show several localized areas of linear settlement outside of the historical Seattle shoreline including the area adjacent to the TBM ingress site. However, no evidence of tunneling induced subsidence was observed. The results demonstrate deformation monitoring in a dense urban setting and show the benefit of InSAR's capability to spatially characterize wide scale deformations. The results were presented to members of the WSDOT SR-99 project team as part of the WSDOT stakeholder workshop. A summary of this workshop is detailed in a separate report.

Lewistown Narrows

LOS deformation estimates were generated for the section of highway along the length of the narrows. Good coherence conditions occurred for the entire highway and some parts of the surrounding slope. However many sections of the slope were incoherent due to vegetation conditions. No significant deformation was observed at any location along the highway. It should be noted that the satellite LOS geometry does not provide good sensitivity to tilting of the retailing wall which runs primarily east-west and therefore the null result is not sufficient to conclude that no tilting is occurring along these sections. The geometry is sensitive to downslope deformation along most sections of the adjacent Blue Mountain slope and these show no significant deformation. A few localized deformations were observed near the Lewistown interchange and also downslope between the eastbound lane and the Juniata River but with LOS velocity magnitudes < 0.01 [ft/yr]. Results from this monitoring site show the potential to monitor extended sections of highway at risk to slope deformations and highlights the geometric limitations of InSAR sensitivity to deformation in the north-south direction.

Bushkill Creek

LOS deformation estimates were generated for the entire Spotlight mode footprint centered on the Route 44 Bushkill Creek Bridge. These results show a high density of coherent points for all areas including roadways, buildings and other areas with the exception of many open fields. Several deformations were observed than can be associated with a variety of causes including mining activities, new building construction, previously emerging sinkholes and slope deformation. Measurements on either side of the Bushkill Creek Bridge were shown to be similar to ground survey results. However, differences in deformation magnitudes were observed which may be due to the fact that vertical only deformation was assumed when making the comparison. Several deforming areas were identified in the part of the scene prone to sinkholes but these do not correspond with any recently reported sinkholes. However these may be precursor deformations and therefore provide value as inputs to sinkhole monitoring activities in the area.

The results from both Pennsylvania sites were presented to members of PennDOT as part of the PennDOT stakeholder workshop. A summary of this workshop is detailed in a separate report.

Geysers

Vertical and east-west deformation estimates were generated by processing and combining data from both pass directions. Despite significant topographic variations in the scene, a sufficient number of targets occurred in both pass directions to spatially characterize deformation in many areas. These results show both vertical and horizontal deformations occurring in the vicinity of known geothermal wells locations. The results over different time periods show deformation fluctuations rather than simply

monotonic behavior which is consistent with cyclical injection. Projection of the deformation onto the local road network shows good coherent point coverage over many roads. These results show that while many secondary roads in the vicinity of the production facilities are deforming, the primary Route 175 is outside the deforming areas. Results from this site demonstrate monitoring extended rural road networks in deformation prone areas include those with significant topographic variation.

THIS PAGE INTENTIONALLY LEFT BLANK

8 REFERENCES

Agram, P. (2010), Persistent scatterer interferometry in natural terrain, Doctoral thesis, Stanford Univ., Stanford, Calif.

Berardino, P., G. Fornaro, R. Lanari, and E. Sansosti (2002), A new algorithm for surface deformation monitoring based on small baseline differential SAR interferograms, IEEE Trans. Geosci. Remote Sens., 40(11), 2375–2383, doi:10.1109/TGRS.2002.803792.

Capolupo A.,S Pindozzi, C Okello, N Fiorentino, L Boccia, Photogrammetry for environmental monitoring: The use of drones and hydrological models for detection of soil contaminated by copper, Science of the Total Environment, 514, 298-306, 2015

Chen, C. W., and H. A. Zebker (2001), Two-dimensional phase unwrapping with use of statistical models for cost functions in nonlinear optimization, J. Opt. Soc. Am. A Opt. Image Sci., 18(2), 338–351, doi:10.1364/JOSAA.18.000338.

Chen, J., H. A. Zebker, and R. Knight (2015), A persistent scatterer interpolation for retrieving accurate ground deformation over InSAR-decorrelated agricultural fields, Geophys. Res. Lett., 42, 9294–9301, doi:10.1002/2015GL065031.

Chen, J., R. Knight, H. A. Zebker, *and* W. A. Schreüder *(*2016*),* Confined aquifer head measurements and storage properties in the San Luis Valley, Colorado, from spaceborne InSAR observations, Water Resour. Res., 52, 3623–3636, *doi:*10.1002/2015WR018466.

Du, Y.,F Ulaby and M Dobson, Sensitivity to soil moisture by passive and active sensors, IEEE Transactions on Geoscience and Remote Sensing, 38(1), pp. 105-114, 2000

Dobson, M. and F Ulaby, , Active microwave soil moisture result, IEEE Transactions on Geoscience and Remote Sensing, 24(1), pp. 23-36, 1986

Dobson, M. and F Ulaby, Preliminary evaluation of SIR-B response to soil moisture, surface roughness and canopy crop cover, IEEE Transactions on Geoscience and Remote Sensing, 24(4), pp. 517-526, 1986

Fedora, M. and R Beschta, Storm runoff simulation using the Antecedent Precipitation Index model, Journal of Hydrology, 112(1-2), pp. 121-133, 1989

Fung, A., Z Li and K Chen, Backscattering from a randomly rough dielectric surface, IEEE Transactions on Geoscience and Remote Sensing, 30(2), pp. 356-369, 1992

Massonnet, D., "The displacement field of the landers earthquake mapped by radar interferometry", Nature, vol. 364, pp. 138-142, July 1993.

Narayan, U.,V Lakshmi and T Jackson, High-resolution change estimation of soil moisture using L-band radiometer and radar observations during the SMEX02 experiments, IEEE Transactions on Geoscience and Remote Sensing, 44(6), pp. 1545-1554, 2006

Panicera, R., M Tanase, K Lowell, J Walker, Evaluation of IEM, Dubois and Oh radar backscatter models using airborne L-band SAR, IEEE Transactions on Geoscience and Remote Sensing, 52(8), pp. 4966-4979, 2014

Waltham T., Bell, F., and Culshaw M (2016), Sinkholes and Subsidence, Springer.

Weary, D J (2015), The cost of karst subsidence and sinkhole collapse in the United States compared with other natural hazards, USGS.

Zebker, H. A., S. Hensley, P. Shanker, and C. Wortham (2010), Geodetically accurate InSAR data processor, IEEE Trans. Geosci. Remote Sens., 48(12), 4309–4321,

ADDITIONAL REFERENCES

R-1 Advanced Space-Based InSAR Risk Analysis of Planned and Existing Transportation Infrastructure - Dual Scale Point Scatterer Analysis Plan. July 14, 2015.

R-2 Eppler, J. and Kubanski, M. 2015. Subsidence monitoring of the Seattle viaduct tunneling project with HDS-InSAR. In Proc. of the Symposium on Field Measurement in Geomechanics (FMGM), Sydney, Australia. 404-414.

R-3 PAMAP—Digital Base Maps for Pennsylvania. Retrieved from http://www.dcnr.state.pa.us/topogeo/pamap/index.aspx on September 15, 2016.

R-4 NOAA-National Center for Environmental Information. Retrieved from https://www.ncdc.noaa.gov/cdo-web/ on August 40, 2016.

R-5 Pennsylvania Department of Conservations and Natural Resources. Retrieved from

http://www.dcnr.state.pa.us/topogeo/field/gsaabstr/gsalist/streammigr/index.htm on September 15, 2016.

R-6 Northern California Power Agency. Retrieved from http://www.ncpa.com/about/generation/geothermal/ on September 15, 2016.

R-7 Power Technology – The Geysers Geothermal Field. Retrieved from http://www.power-technology.com/projects/the-geysers-geothermal-california/] on September 15, 2016.

R-8 Pennsylvania Spatial Data Access Portal. Retrieved from http://www.pasda.psu.edu/uci/SearchResults.aspx?originator=Pennsylvania+Department+of+Transportation on August 40, 2016.

R-9 Lake County GIS Portal. Retrieved from http://gispublic.co.lake.ca.us/portal/home/gallery.html#c=organization&f=layers-layerfiles&o=modified on August 40, 2016.

R-10 Sonoma County GIS Portal. Retrieved from https://links.sonoma-county.org/nIhrCoQbqzY/ on August 40, 2016.

R-11 Calpine – The Geysers Portal. Retrieved from http://www.geysers.com/map.aspx on August 40, 2016.